Characterization of Construction Material Properties through Gamma Spectroscopy, X-ray Fluorescence, and Hyper-spectral Imagery for Background Correction Applications in Nuclear Detection

THESIS

Jared D. Casebolt, Captain, USAF

AFIT-ENP-14-M-45

DEPARTMENT OF THE AIR FORCE
AIR UNIVERSITY

AIR FORCE INSTITUTE OF TECHNOLOGY

Wright-Patterson Air Force Base, Ohio

AFIT-ENP-14-M-45

CHARACTERIZATION OF CONSTRUCTION MATERIAL PROPERTIES THROUGH GAMMA SPECTROSCOPY, X-RAY FLUORESCENCE, AND HYPER-SPECTRAL IMAGERY FOR BACKGROUND CORRECTION APPLICATIONS IN NUCLEAR DETECTION

THESIS

Presented to the Faculty

Department of Systems and Engineering Management

Graduate School of Engineering and Management

Air Force Institute of Technology

Air University

Air Education and Training Command

In Partial Fulfillment of the Requirements for the

Degree of Master of Science in Systems Engineering

Jared D. Casebolt, BS

Captain, USAF

March 2014

AFIT-ENP-14-M-45

CHARACTERIZATION OF CONSTRUCTION MATERIAL PROPERTIES
THROUGH GAMMA SPECTROSCOPY, X-RAY FLUORESCENCE, AND HYPER-
SPECTRAL IMAGERY FOR BACKGROUND CORRECTION APPLICATIONS IN
NUCLEAR DETECTION

Jared D. Casebolt, BS
Captain, USAF

Approved:

_____//signed//_____   14 Mar 2014
David J. Bunker, Ph.D. (Chairman)   Date

_____//signed//_____   14 Mar 2014
Tay W. Johannes, Ph.D., Lt Col, USAF (Member)   Date

_____//signed//_____   12 Mar 2014
Benjamin R. Kowash, Ph.D., Maj, USAF (Member)   Date

AFIT-ENP-14-M-45

Abstract

Material identification through hyper-spectral imagery provides a potentially useful data input for background radiation prediction models for gamma spectrum correction in mobile nuclear detection applications. Traditional background correction methods which rely on prior information are often impractical in mobile detection. Prediction models could combine material information with spatial data to develop a suitable substitute to actual background radiation measurements.

This research investigates the relationship hyper-spectral properties and natural radioactivity of construction materials. A selection of construction materials are analyzed using three instrumentation methods: 1) gamma-spectroscopy, 2) X-ray fluorescence (XRF), and 3) hyper-spectral imagery. Gamma-spectroscopy focuses on the presence of potassium as well as uranium and thorium series progeny through analysis of ^{212}Pb, ^{214}Pb, ^{214}Bi, and ^{228}Ac signature peaks. XRF analysis provides the chemical composition of each material. Each materials hyper-spectral characteristics are compared to chemical composition and radioactive properties to determine if any identifying features relate to natural radioactivity.

To my mother and father

Acknowledgments

To my Thesis Advisor, Dr. David Bunker, thank you for your patience and guidance through the final stages of this project.

To my other Thesis Advisor, Maj. Benjamin Kowash, thank you for the inspiration and motivation in the development of this project.

To the experts; Lt Col Tay Johannes, Dr. Christopher Borel-Donohue, and Dr. Larry Burggraf, thank you for the guidance and corrections along on the way.

To Mr. Eric Taylor, thank you for your patience with my material stockpile in the laboratory and for your help with the instruments.

Jared D. Casebolt

Table of Contents

List of Figures

List of Tables

List of Equations

TITLE

I. Introduction

General Issue

The United States (U.S.) has a vital interest in preventing nuclear terrorism. When the Nuclear Posture Review was released in 2010, President Barack Obama stated "the greatest threat to U.S. and global security is no longer a nuclear exchange between nations, but nuclear terrorism by violent extremists and nuclear proliferation to an increasing number of states" (Obama, 2010). In order to conduct a nuclear terrorism attack, violent extremists must obtain special nuclear material (SNM) and transport it to the attack location. Attack prevention measures focus on SNM inventory control, production control, and illicit transportation interdiction. Authorities can use radiation detection systems to detect, identify, and locate SNM. Radioisotopes can be located and identified using gamma-spectroscopy. However, naturally occurring radiation complicates spectra collected in the field. A spectrum can be corrected if information about the background radiation is known. Unfortunately, this prior information on background radiation is not always available. A methodology for estimating background radiation based on available information could improve detection accuracy and quickness.

Radiation detection system capabilities vary by system type. Very basic systems can alert the operator only to the presence of some form of radioactive source. Using advanced systems, an operator can identify specific radioisotopes and even determine the location of the source. Detection systems can be static or mobile. Static

detectors are typically used at major transportation hubs. Referred to as portal monitors, these static detectors are used to inspect vehicles and containers as they pass through the hub (Lo Presti, 2006).   The portal monitor concept relies on the assumption that smugglers will attempt to transport SNM through one of these hubs. The cost of building a static detector network large enough to account for all other possible smuggling routes is prohibitively expensive. Mobile detection systems are able to search large areas with fewer detectors than static alternatives.   Therefore, the mobile approach is more practical for large area applications (Cheng, 2009).

Mobile radiation detection research has largely focused on two methods. One method relies on a small number of vehicles equipped with multiple sensor types and high resolution detectors. These systems combine high sensitivity detectors for radioisotope identification with coded aperture detectors for locating sources (Mitchell, 2009). The other approach is to leverage common vehicles, such as taxi cabs, to create a large network of sensors. These systems rely on the small, simple detectors to detect the presence of SNM (Cheng 2009).

The Mobile Imaging and Spectroscopic Threat Identification (MISTI) platform is a mobile radiation detection system. This system is based on the concept of bundling a variety of sensors onto a small number of vehicles. A MISTI vehicle carries a ten by ten sodium iodide detector array with a coded aperture for imaging. Spectroscopy capability, for radioisotope identification, is provided by 28 HPGe detectors (Mitchell, 2009). Additional sensors include: lidar, infrared cameras, visible light cameras, and a weather station (Aucott, 2013).

Gamma-ray spectroscopy can be used to identify a gamma-ray's source radioisotope. All radioisotopes undergo a natural decay process. As individual atoms decay, electrons seek higher energy levels. Because energy is conserved, energy is emitted from the atom when an electron moves to a higher energy level. In the case of gamma decay, energy is released in the form of photons. Each radioisotope has a unique decay scheme and produces gamma-rays at specific energy levels. This gamma radiation can be detected using plastic scintillators, sodium iodide NaI(Th) scintillators, or high purity germanium (HPGe) semiconductors. For each of these types of detectors, photons enter the detector and cause photoelectric, Compton scatter, or proton annihilation interactions. As photon interactions occur within the detector, the device produces voltage pulses based on the energy of the interaction. A multichannel analyzer assigns each pulse to a channel based on the voltage pulse and counts the number of occurrences in each channel to produce a spectrum. As the number of counts in each channel increases, a spectrum of photopeaks emerges. Radioisotopes are identified by matching the photopeak energy levels to known decay schemes. When a photon produces a Compton scatter interaction, a portion of the photon's energy is imparted to a free electron in a collision. The amount of energy imparted to the electron is dependent upon the angle of the collision. As a result, the detector will register at least two photons at lower energy levels than the gamma-ray emitted by the source. Multiple Compton scatter interactions create the Compton continuum. This continuum is a region of counts registered at lower energy levels than the full energy of the original photons. Detector efficiency is dependent upon the solid angle geometry of the source and the detector. A source will emit ionizing radiation in all directions, but the detector can count only the

3

radiation which enters and interacts within the detector. As the distance between the detector and the source increases, fewer gamma-rays are successfully counted in the detector. Scintillators convert interactions to voltage pulses less accurately than semiconductors. As a result, semiconductors provide higher resolution. At lower resolutions, the photopeaks are wider and more likely to overlap (Knoll, 2010).

Research Objectives

SNM is not the only source of ionizing radiation in the natural environment. Gamma-rays are produced by charged particles from cosmic rays, naturally occurring thorium or uranium series progeny, and potassium (UNSCEAR, 1993). These sources contribute to the background radiation and can obscure SNM signature peaks in the spectra. When background radiation is present, numerous sources produce signature photopeaks. Each of these photopeaks is accompanied by a Compton continuum. Wide photopeaks, a result of low resolution, merge with other peaks and the continuums (Knoll, 2010).

The presence of background radiation sources varies from location to location. Background spectra changes as a mobile detector move from one location to another. With prior knowledge of the background radiation, spectral correction techniques can isolate SNM sources and improve detection results. However, this prior information is not always available. A methodology for estimating background information could allow detection system designers to apply spectra correction techniques based on available information such as time of day, precipitation, and building materials in the surrounding area. This information could be used to optimize gamma-ray detector deployment to

4

increase the probability of detecting SNM. This research will investigate relationships between gamma spectra collected from terrestrial background radiation sources and hyper-spectral spectra. If valid relationships exist, they could be used to characterize background radiation and predict background levels based on alternative sensor data such as optical or hyper-spectral imaging. The methodology for collecting the spectra and analyzing the relationships is presented in Chapter III.

Assumptions and Limitations

Equipment and material availability limited this study.   Construction material samples were acquired locally at little or no cost. As a result, the number of samples is limited. Powder samples for XRF analysis were extracted from the samples with a drill bit and prepared in sample cups. Particle size and consistency cannot be controlled through this method. XRF results could be improved by producing the powder in ring grinder and pressing the powder into pills if the equipment is available. Hyper-spectral measurements were collected with a point of source instrument. The spectral range of this instrument is appropriate considering the proposed spectroradiameter for MISTI. However, complications such as solar radiance, shade, and surface angle were avoided by collecting data indoors using a hand probe and well-characterized illumination lamp.

II. Literature Review

Chapter Overview

   Static portal monitors and mobile detectors are tools for detecting nuclear material. Both are elements of a layered approach to smuggling interdiction. Portal monitors are adequate for traffic hubs such as ports and border crossings. Outside of areas where traffic can be highly channelized, mobile detectors are more useful search tools. A common radiation detection method is gamma spectroscopy. Whether employed in a static or dynamic role, the nature of detection efforts requires the gamma-ray detectors to be exposed to naturally occurring background radiation. This background radiation can originate from cosmic rays or natural materials in the detector's surroundings. The radiation emitted from natural sources can obscure the signature of the material of interest. This chapter reviews recent work on nuclear detection systems to examine how researchers approach the influence of background radiation. Next, the principles of gamma-spectroscopy are reviewed to highlight the fundamentals of the background radiation problem. Finally, the features of the MISTI vehicle are provided.

2.1 Detection Systems

   Location and identification of nuclear material requires detectors and a means of interpreting detector data. This section reviews research data analysis. The goal of detector data analysis is to identify a specific source signal over the noise created by the background. When the analysis identifies a source, and a source is present, the desired result is an alarm. The alternative states are false positives, alarms when no source is present, and false negatives, no alarms when a source is present. Cheng developed a

multiple spatial cluster model for networked mobile detectors. Included in this model is a function for background variation. One proposal is to base the background function on historical data. Another proposal is to calculate the function with knowledge of the radiation emitting materials along the route (Cheng, 2011). Dimitrov used parametric methods for determining alarm probabilities to improve upon transport code calculation times. Background is represented in his equations based on an assumption of the average terrestrial background in the United States (Dimitrov, 2009). Liu investigated an algorithm which combines of parametric estimation and Bayesian calculations. Background radiation parameter estimates for this study are based on historical survey data. Background is assumed to be uniform across small areas and variable across large areas containing radiation emitting material. The survey data show background ranges of 500 to 1200 counts per second. Liu's algorithm attempts to estimate background sectioning the area into cells and averaging the count rates of the detectors with the lowest count rate in each cell (Liu, 2011). Novikova developed a model for predicting background spectra for use in Monte Carlo simulations. The model is useful for detector system design; however, the coefficients must be scaled to each location (Novikova, 2007). As researchers approach the problem of detector data analysis, they employ a variety of methods for reducing noise produced by background radiation. These methods rely heavily on assumptions, which indicate a need for better understanding about the nature and behavior of background radiation. Background radiation parameters based on estimates derived from information gathered from the detector's surroundings at the same time as gamma-ray recordings may improve the accuracy of SNM search algorithms.

Hyper-spectral material identification on surrounding materials would provide additional information which could be used to produce background estimates.

2.2 Principles of Gamma Spectroscopy

An understanding of gamma-spectroscopy must be established to understand the problems caused by background radiation in detector data. Plastic scintillators, sodium iodide (NaI) scintillators, and high purity germanium (HPGe) semiconductors are commonly used for nuclear material detection. This section summarizes essential concepts of gamma-spectroscopy as presented by Knoll. Gamma-spectroscopy is the use of a detector to convert energy from photons into voltage pulses. Photons are emitted by decaying radioisotopes. As radioisotopes decay, electrons move from low energy states to higher energy states. To conserve energy, a photon is emitted at an energy level equal to the change in electron energy state. These photons interact with detector material. In plastic scintillators, the interaction takes place within a polymer material. In NaI detectors, the interactions take place within a NaI crystal. HPGe detectors use a germanium semiconductor. Photon interactions in scintillators produce flashes of visible light which are converted into voltage pulses. In semiconductors, photons cause free electrons to cross the valance and fill electron holes. The movement of the electrons translates into a voltage pulse.

When a photon enters a detector, an interaction takes place with the detector material. If the interaction is photo-electric, the photon collides with an atom and frees an electron. This electron has the same energy as the original photon, and the photon's energy is successfully converted to a voltage pulse. In some cases, the photon collides

with a free electron rather than an atom. This interaction creates Compton scatter. A portion of the photon's energy is converted to a voltage pulse and the photon continues to travel through the detector.   As it continues, the photon causes additional interactions at lower energy levels or escapes the detector. When a photon escapes the detector, the energy is not recorded. An accumulation of counts at reduced energy levels as a result of Compton scatter is known as the Compton continuum.   In a third type of interaction, a photon creates a positron-electron pair within the detector. The positron annihilates and produces two gamma rays at 511 kiloelectron volts (keV). One or both of these new gamma rays may cause additional interactions or escape the detector. This interaction is known as pair production. Pair production is recognizable in the spectrum by the appearance of peaks at 511 keV and 1022 keV.   As photons interact with the detector and create voltage pulses, a count is made of each pulse at each voltage. The voltages are assigned to channels. A plot of counts against channels reveals the spectrum.

Photons travel from a source to the detector face through a space defined by cone shaped region. The angle of this cone is referred to as the solid angle. The probability that a photon emitted from the source will enter the detector increases as the solid angle increases (Knoll, 2010).

Detector interactions and physical limitations which produce error in gamma spectra are complicated further in mobile detections. Count times are limited and natural radiation sources introduce photons with a wide range of energy levels.

2.3 Background Radiation

Natural sources of gamma rays include decaying isotopes and cosmic flux. Natural radioactive isotopes occur in widely used construction materials. Zaidi measured the activity of uranium (^{238}U) and thorium (^{232}Th) in sand, clay brick, Portland cement, and soil (Zaidi, 1999). Potassium (^{40}K) is another common radioisotope (UNSCEAR, 1999). Some isotopes, such as cesium (^{137}Cs), have very simple decay schemes which produce gamma rays at a single energy level. In a spectrum, ^{137}Cs produces a single peak at 662 keV. More complicated decay schemes produce gamma rays at over a dozen energy levels (Ekström, 2004). A high resolution detector will produce a spectrum with identifiable peaks. Detector resolution is measured in terms of the full width at half maximum (FWHM) of the prominent peak (Knoll, 2010). In a scintillator detector, the FWHM can grow so large that the peaks begin to overlap. Each peak has an associated Compton continuum which overlaps in a crowded spectrum. A source can be obscured in the noise of a crowded spectrum as a result of background radiation. This problem is compounded when the detectors solid angle geometry with a strong background emitter creates higher efficiency than the geometry with the source (Ziock, 2004). Physical barriers, such as a building or a vehicle, can shield the source from the detector. Shielding also affects false positive rates when a detector is temporarily shielded from a large fraction of the background (Lo Presti, 2006). Construction materials emit and shield gamma-rays.

Construction Materials

The primordial radionuclides and their progeny occur naturally in soil and rocks. These naturally radioactive materials are incorporated into building materials produced

from soil and stone. Portland and asphalt concretes contain stone aggregates and sand.

Bricks are formed from clays. Certain rock formations have been found to contain higher

levels of natural radiation. In general, igneous rock formations are more radioactive than

sedimentary rock formations (Tzortzis, 2003). The radioactive properties of construction

materials are dependent upon the region in which their components were quarried.

Because of their associated cure times, Portland and asphalt concretes are usually

produced locally. The radioactive properties of these materials should reflect those of the

region in which the end product is found. Finished products such as Concrete Masonry

Units (CMU) and bricks are easier to transport over large distances, and the products

encountered in a region of interest may not have originated locally. Determining the

source of construction materials encountered in a region of interest is no simple task.

However, the chemical properties of the material may provide a means of estimating a

materials radioactivity.

<center>Portland Concrete Cement</center>

Portland Concrete Cement is produced by mixing Portland cement with sand,

water, and stone aggregate. Portland cement is produced by heating raw materials to

produce clinker. This clinker may contain the chemical compounds shown in the

following list (Chen, 2003).

1. Tricalcium aluminate ($3CaO\ Al_2O_3$)

2.   Tricalcium silicate ($3CaO\ SiO_2$)

3. Dicalcium silicate ($2CaO\ SiO_2$)

4. Tetracalcium aluminoferrite ($4CaO\ AlO_3\ Fe_2O_3$)

5. Sodium oxide (Na_2O)

<center>11</center>

6. Potassium oxide (K_2O)

Portland cement may be blended with pozzolan admixtures to meet certain design requirements. Admixtures include blast furnace slag, low-lime fly ash, high-lime fly ash, and silica flume. Chemical compositions of these admixtures and Portland cement are shown in Table 1 (Philleo, 1989).

Table 1: Typical Composition of Cementing Materials (Philleo,1989)

% by Mass	Portland Cement	Blast Furnace Slag	Low-lime Fly Ash	High-lime Fly Ash	Silica Flume
CaO	63	40	1	20	0
SiO_2	22	35	50	35	90
Al_2O_3	6	8	25	20	2
Fe_2O_3	3	0	10	5	2

In the formation of concrete, the cementious materials react with water in two ways. First, the aluminates react with water to produce calcium mono-silicate. Calcium silicates react with water to produce calcium hydroxide. Next, calcium hydroxide reacts with silicates in the pozzolans to produce calcium silicate hydrates (Chen, 2003).

The chemistry discussed to this point represents only the cement paste within the concrete. Portland cement, pozzolans, and water account for approximately 20% of the weight by volume of a concrete mix. The remaining portion of the concrete mix is comprised of sand and stone aggregates (Chen, 2003). Aggregates and sand are typically specified by physical properties such as size, durability, and hardness. These materials are selected based on regional availability and their chemical composition could be expected to vary.

Concrete Masonry Units

Concrete Masonry Units are pre-formed Portland concrete blocks. The blocks are assembled into a structure with mortar in a similar fashion to brick. CMU blocks may be hollow. Structural designs may call for these hollow units to be filled with grout. As a result of these variations in unit design and application, it is difficult to determine the composition of a CMU structure by visual inspection. Grouts and mortars employ similar cementing materials to those shown in Table 1. Grout, mortar, and Portland cement in CMU rely on the same hydration and pozzolan reactions to develop strength, and their chemistry can be expected to be similar. Differences in aggregate and sand may influence the radioactivity of the structure. Grouts and mortars, in a similar fashion to Portland cement, are likely produced with local materials due to cure times. These materials also contain more sand than aggregate.

Asphalt Concrete Cement

Asphalt concrete cement (ACC) is produced by mixing a petroleum based binder with sand and gravel aggregates. The petroleum binder is refined from crude oil. The sand and gravel may comprise 90-95% of an ACC mix by weight. (Asphalt Institute, 2003). Typically used for paving, ACC is placed while the binder is heated to viscous state. The material gains strength as the binder cools and solidifies. This process is time sensitive. As a result, it is likely that ACC is produced from local sands and aggregates. These sands and aggregates have similar requirements to those used in Portland concrete. A key difference is that ACC aggregates bind to asphalt and resist the interference of moisture in the binding process. Calcareous material such as limestone and dolomite

tend to bind more effectively than siliceous materials like quartz and granite (Asphalt Institute, 2003).

Clay Brick

Clay brick is produced from a mix of sand, silt, and clay. The material is formed into bricks and fired in a kiln. Table 2 shows the results of an XRF analysis of raw clay powder performed by Gredmaier, Banks, and Pearce. The powder sample was pressed into pellets for analysis (Gredmaier, Banks, & Pearce, 2011).

Table 2: Raw clay powder XRF analysis (Gredmaier, Banks, & Pearce, 2011)

Compound	% by weight
SiO_2	66.2
TiO_2	0.95
$Al2O_3$	19.13
Fe_2O_3	8.08
MnO	0.03
MgO	2.15
CaO	0.5
K_2O	2.94
Na_2O	0.15
P_2O_5	0.08

Steel

Steel is an iron and carbon alloy. It is produced by heating smelted iron ore to reduce carbon to specific amounts. Steel may be hot rolled or cold rolled to produce structural building components. Common structural steel grades in the United States are American Society for Testing and Materials (ASTM) specification A992, A36, and A572 Grade 50 (Cheng, 2003). The following chemical requirements for A36 steel are provided in ASTM A36/A36M-97a as shown in Table 3.

Table 3: A36 Steel Chemical Requirements
(ASTM A36/A36M-97a)

Carbon, max, %	0.26
Manganese, %	-
Phosphorous, max, %	0.04
Sulfur, max, %	0.05
Silicon, max, %	0.4
Copper, min, %, when specified	0.20

Stainless steel is produced by alloying carbon steel with additional elements such as nickel and chromium. The certified range of elemental concentrations in some stainless steel samples are shown in Table 4.

Table 4: Certified Concentrations in Stainless
Steel Samples, (Tiwari, Singh, and Sawhney, 2001)

Chromium, %	16-20
Manganese, max, %	2.0
Iron, %	60-70
Nickel, %	8-14
Copper, %	-
Niobium, %	-
Molybdenum, %	0-3

2.4 X-ray Fluorescence

The natural radioactive properties of construction materials are determined by their elemental composition. X-ray fluorescence is one technique for elemental analysis. Elements are identifiable by their characteristic X-rays. To produce characteristic x-rays, photons are directed at the sample. These photons interact with atoms within the sample to excite electrons and produce vacancies in the atomic shells. When the atom de-excites, electrons move within the shells to fill vacancies. As electrons move to higher energy positions, characteristic X-rays are produced to conserve energy and momentum. From

this point, X-ray fluorescence is similar to gamma-spectroscopy. Characteristic X-rays emitted by the sample are collected by a semiconductor detector. A multichannel analyzer counts voltages pulses produced by X-ray interactions within the semiconductor (Dzubay, 1977).

2.5 Hyper-spectral Imaging

Hyper-spectral imaging is a method for identifying materials based on their reflective, absorptive, and emissive properties with regards to photons across multiple spectral ranges (Clark, 1999). Spectral ranges include ultraviolet, visible, and infrared. These ranges have been defined by photon wavelengths. The instrument used in this study detects photons in the visible range at 350 to 700 nm and the near infrared range at 700 to 2500 nm. Photons are absorbed or reflected by a material surface. Some materials may allow the photons to pass through. Natural surfaces emit photons at temperatures above absolute zero (Clark, 1999). The result of interactions of the material surface and photons provides identifying information about the materials texture and composition (Clark, 1999).

2.6 Mobile Imaging and Spectroscopic Threat Identification (MISTI)

The Mobile Imaging and Spectroscopic Threat identification (MISTI) vehicle is unique because it combines multiple sensors into one system. Mitchell describes the MISTI vehicle capabilities. The vehicle combines a NaI coded-aperture large area imager array with an HPGe high resolution spectrometry array. The large area imager provides source location capability. The resolution of the HPGe array allows for source identification. The vehicle carries liquid nitrogen dewars to cool the HPGe array.

16

Additional sensors include infra-red and visible light cameras, lidar, a weather station, and Global Position System (GPS) (Mitchell, 2008). Data collected from MISTI experiments have been studied by Huh and Aucott. Huh investigated the ability to track moving sources with the vehicle's coded-aperture imager (Huh, 2012). Aucott explored variation in background levels by region type (Aucott, 2013). The addition of a hyper-spectral sensor to identify surrounding materials for the purpose of background radiation has been proposed. However, the method for translating hyper-spectral data into usable background radiation information has not been developed.

Conclusion

Background radiation presents a problem for mobile detection system design and data analysis. Mobile detection is always conducted in the presence of naturally background radiation from cosmic radiation and terrestrial isotopes. The MISTI vehicle provides a unique platform of sensors for mobile detection. The vehicle collects imaging for localization and high resolution spectra for identification at the same location at the same time. The performance of the MISTI detectors may be improved by correcting the spectra for background contributions. The radiation background in urban areas includes gamma emissions from natural radioactive isotopes in construction materials. The radioactivity of these materials is dependent upon the radioactivity of the materials from which they are produced. The chemical composition of the materials may indicate their source and their natural radioactivity. The materials chemical composition may also influence the hyper-spectral signature. If so, it may be possible to estimate background

radiation with material identification information obtained from hyper-spectral imagery

and geometric information provided by lidar.

III. Methodology

Chapter Overview

As a detector is moved through a search area, the level of background radiation will change. Each change in background radiation will impose some change in the detector's point source detection accuracy. Two background radiation sources are cosmic rays and naturally occurring radioactive materials. Using hyper-spectral imagery, it is possible to determine the types of material in the detector's search area. A prediction model based on hyper-spectral material identification and predetermined material background contribution factors allows for real time background correction. This chapter provides a methodology for collecting and comparing the background contribution of common construction materials. The equipment and procedures for collecting background measurements from sample materials are presented first.

3.1 Materials

The materials samples selected for this study represent a variety of common construction materials. These materials include asphalt concrete cement, Portland concrete cement, concrete masonry units, brick, and structural steel. The ACC and PCC samples were retrieved from construction waste piles. The brick, CMU, and steel samples were obtained through local material suppliers. In order to maintain consistent geometry for gamma spectroscopy, each material sample was trimmed to the size of two standard red bricks.

3.2 Gamma Spectroscopy

Gamma-ray emission measurements were collected using an Ortec® Detective-EX 100S P-type coaxial high purity germanium (HPGe) portable detector. The Detective-EX has an integrated multichannel analyzer (MCA) and Global Position System (GPS). The detector can be controlled remotely by means of a Universal Serial Bus (USB) connection. For this experiment, the detector was connected to a laptop computer running Ortec® GammaVision® software. Energy calibration was accomplished with an eleven peak multi-nuclide planchette positioned on a manufacturer provided calibration stand. The energy calibration curve is shown in Figure 1.
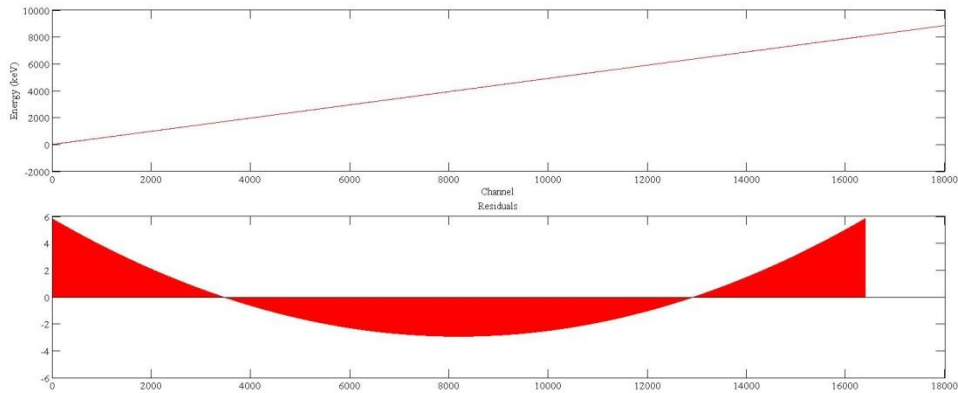
Figure 1: Energy Calibration with Linear Fit and Residuals

Efficiency calibration was not possible due to the lack of certified standards which matched the sample material geometry. The detector was fitted with a lead collimator. Within the collimator, a thin copper layer shields the primary lead layer. The layers of the collimator are shown in Figure 2.

20
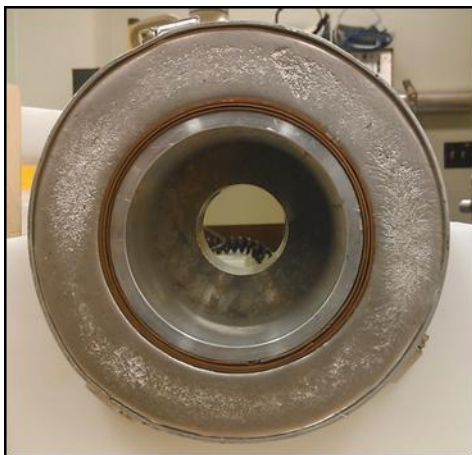
Figure 2: Collimator

The Detective-Ex was equipped with a neutron detector. The neutron detector

and cover were removed to accommodate the collimator. The experiments were

conducted within a cave constructed of lead bricks to reduce background counts. The

detector was powered through an adapter which was also placed inside of the cave. The

detector is shown inside of the lead cave in Figure 3.

Figure 3: Detective-EX in lead cave
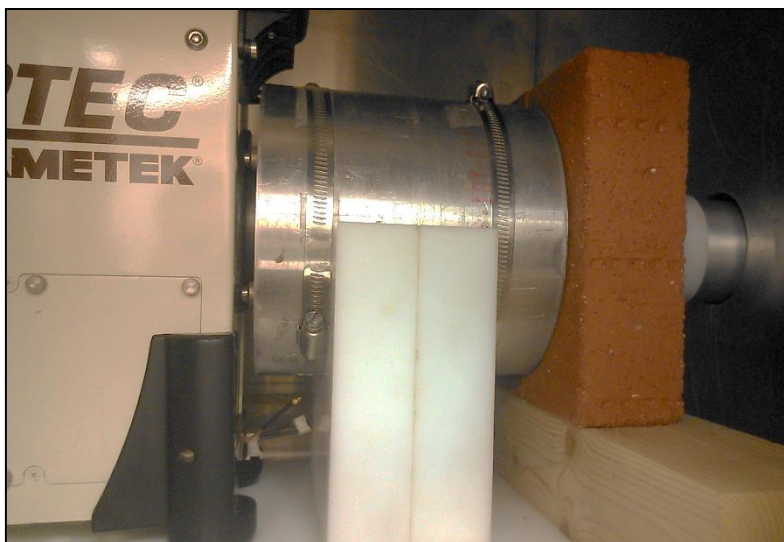
Figure 4: Detector with Sample

Five initial background measurements were taken for 86,400 seconds. Additional background measurements were taken throughout the series of experiments. Material samples were placed directly in front of the detector against the face of the collimator. Figure 4 shows the position of the material sample during measurement. Counts were recorded for 86,400 seconds real time for each measurement. The spectra were analyzed with GammaVision® version 6.08. Peaks were located using the blind peak search function. Exported files included the peak analysis results and spectrum. The net peak area from the peak analysis was used to calculate a weighted best value for each region of interest.

3.3 X-ray Fluorescence

The material samples in this study were examined with X-ray fluorescence to determine their chemical compositions.   This elemental analysis provides a link between the hyper-spectral and radioactive properties of the material. For example, a material

which has a hyper-spectral signature indicating the existence of minerals which are known to be associated with higher concentrations of uranium, thorium, or potassium would be expected to have higher radioactivity.

An XRF elemental analysis was performed on each material sample. The metal samples were assumed to have an adequate level of elemental homogeneity to be prepared in plate form. A thin plate was cut from each metal block. The red brick, concrete, asphalt, and sandstone samples were prepared for XRF analysis in powder form. This was done to increase the accuracy of the bulk material analysis by reducing the impact of aggregates in the material. Powder samples were retrieved using a $5/8^{th}$ inch drill bit. The material extracted by the drill bit was collected in labeled bags. The equipment was cleaned between each extraction to reduce cross contamination. The bags were turned several times to evenly distribute the particles. Powders were then taken from the bags and placed in 32 millimeter by 23 millimeter Chemplex™ sample cups. The equipment and work surface were cleaned between each sample preparation to reduce cross contamination. The sample cups were sealed using Chemplex™ 1.5 micrometer ultra-polyester x-ray film. Each sample was analyzed using a Horiba XGT-7000. After a sample cup or plate was placed in the machine, the test compartment was vacuumed. The Horiba XGT-7000 allows for a 10 micrometer or 100 micrometer x-ray beam aperture and variable voltage and current. The x-ray tube has a Rhodium target. The instrument contains a high purity silicone detector. Element detection is limited to an atomic number range of $11 < Z < 92$. With no means of measuring particle size or access to ring grinding equipment, instrument settings were selected based on a worst case particle size assumption. The beam aperture was set to 100 micrometers. Measurements

were taken at 12 points across the sample surface in a three by four array. Horiba recommends 20% to 30% detector dead time for measurements taken with the XGT-7000. Current was set to automatically adjust to maintain a dead time within this range throughout each of the tests. The x-ray tube voltage was set to 50 kV to capture the widest range of potential elements in each sample. Each measurement was collected over a 120 second live time. This counting time was selected to balance the time required for peaks to resolve with time constraints on the experiment. At the end of each test, spectrum and quantification data were collected. Quantification data was produced using the fundamental parameters method with the Horiba software. The procedures for the XRF experiments are provided in Appendix B.

3.4 Hyper-spectral Imagery

Hyper-spectral measurements were made on each material sample using an Analytical Spectral Devices (ASD) FieldSpec ® spectroradiometer. This instrument has a visible and near infrared (Vis/NIR) range of 350 to 2500 nm (ASD Website).   The subject sample was illuminated using an ASD Model A122300 hand probe with a halogen bulb. The instrument was calibrated using a manufacturer provided reference white disc. The reference disc was placed inside of the hand probe cap. A measurement was then taken with the cap in place on the hand probe.   By selecting the WR option in the ViewSpec™ Pro 5.6 software, reflectance from the reference disc was set to 1.0 across the spectral range of the device. This calibration may drift over time if the fiber optic cable is not firmly seated in the hand probe. Because of this, a new calibration was accomplished at each sample material change. Measurements were taken on a naturally

24

exposed face of each material block rather than fresh cut faces. For each sample, the

block face was divided into thirds, and one measurement point was selected from each

third. Figure 5 illustrates the test locations. This was done to capture any variation from

weathering effects or architectural color gradations in the samples.
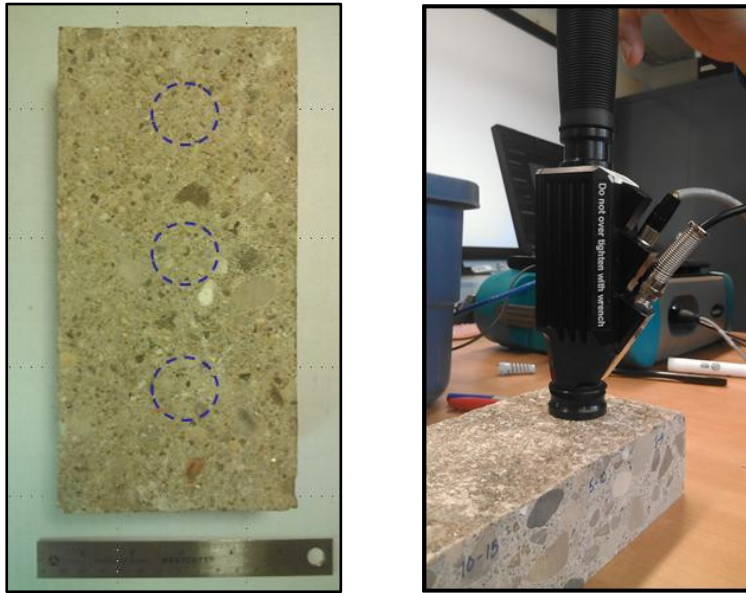
Figure 5: Left: Illustration of ASD Test Locations Right: ASD Hand Probe
Applied to Material Surface

The hand probe was held firmly in place while the measurements were recorded.

If the hand probe is not held firmly and consistently, outside light will infiltrate the

contact edges of the probe and corrupt the measurement. Five measurements were taken

at each test point.   The data was plotted in MATLAB for visual comparison. The

differences between the various spectra were quantified by calculating the angle between

the spectral vectors. Angles were determined by calculating the dot product of two

vectors as shown in Equation 1 (Zill & Cullen, 1998).

$$\cos\theta = \frac{\boldsymbol{a} \cdot \boldsymbol{b}}{\|\boldsymbol{a}\|\|\boldsymbol{b}\|} \tag{1}$$

Where:

θ = Angle between two vectors

$\boldsymbol{a}$ and $\boldsymbol{b}$ = vectors

Conclusion

The purpose of this study is to evaluate the material hyper –spectral and radioactive properties of construction materials. Reliable relationships between a material's hyper-spectral properties and natural radioactivity must be established in order to translate hyper-spectral information into usable background prediction model inputs. Radiation and hyper-spectral measurements were conducted on a variety of construction materials. The results of these measurements were then analyzed and compared in an attempt to identify relationships between the hyper-spectral and radioactive properties. The chemical compositions of the materials were determined through XRF analysis. The purpose of the XRF analysis was to provide supporting evidence to any usable link between hyper-spectral properties and radioactivity.

IV. Analysis and Results

Chapter Overview

Data from each instrument were first analyzed separately. The results of these separate analyses were then compared against each other. This chapter is arranged in a similar fashion. First, the analysis and results of the gamma spectroscopy results are presented. This is followed by the XRF results. The hyper-spectral plots and analysis for the materials are presented next. Finally, the results of the experiments are brought together.

4.1 Results of Gamma Spectroscopy

Background Analysis

Over the course of this study, 13 background measurements were made within the lead cave with the Ortec® Detective-Ex. Of these test, five were conducted before any samples were measured. The collection time for each background measurement was 86,400 seconds. Each background spectrum was analyzed using GammaVision®. Peaks were identified using the blind peak search function within the software. Reports of these peak searches include the peak energy centroid, FWHM, gross counts, and net counts. Figure 6 shows the net peak area for all peak energies which accumulated over 100 counts in any of the background measurements.
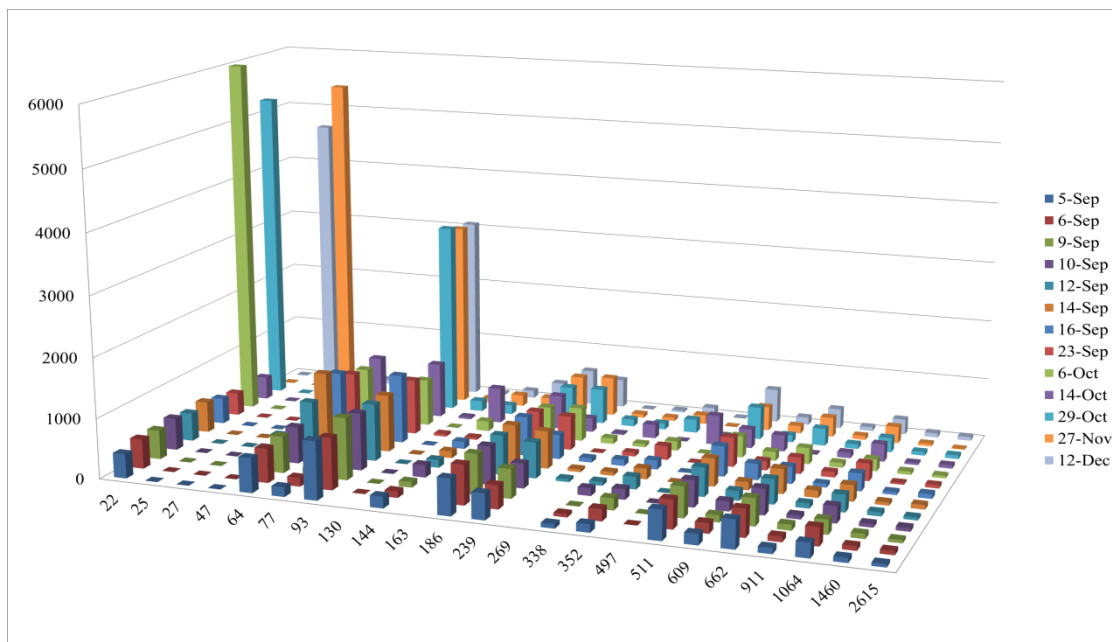
Figure 6: Background Net Peak Counts by Energy (KeV) by Test Date

From this data, seven peak areas stand out as anomalies. The largest is the 22 keV peak from measurement taken on 6 October with a net peak area of 219,655 counts. The dead time for this test was 0.0004%. The mean net peak area at 22 keV had been 478.8 counts with a range of 405 to 534 counts over the five initial background tests. The difference between the 6 October background and a background without the large peak at 22 keV is shown in Figure 7.
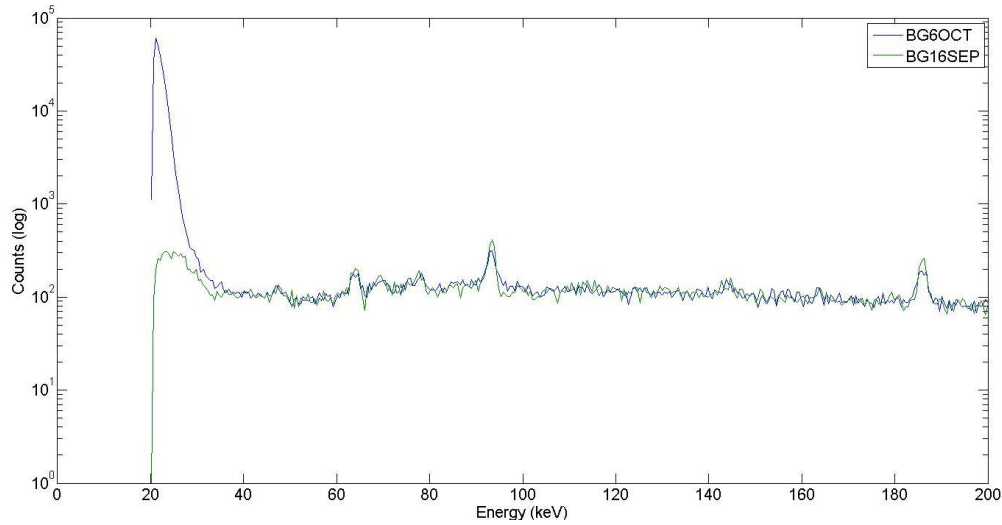
Figure 7: Comparison of background spectra from 6 October (blue) and 16 September (green)

While the 22 keV peak is located in a spectral region which is influenced by characteristic X-rays and coincidence summing, it is doubtful that these effects could account for this 47,098% increase in peak area counts. This background test took place after the final test on Red Brick #3. The anomaly appears in one other measurement. During the 29 September test for Red Brick #3, 252,771 counts were recorded in the net peak area at 22 keV. Contamination from the sample does not appear to have caused the drastic spike in background because only 1320 counts were recorded in the 22 keV peak during the final test of Red Brick #3. The seven anomalous observations and tendencies over the first five background tests are shown in Table 5.

Table 5: Background Measurement Anomalies

Test Date	Peak Energy (keV)	Net Peak Area	Mean Net Peak Area*	Standard Deviation*
6 October	22	219,655	478.8	46.912
29 October	22	5260	478.8	46.912
29 October	93	3213	953.8	60.28
27 November	47	5473	117.2	118.86
27 November	93	3102	953.8	60.28
12 December	25	4649	0	0
12 December	93	3075	953.8	60.28
*Over first five background tests				

The specific regions of interest for sample analysis were the 239 keV peak for ^{212}Pb, 352 keV peak for ^{214}Pb, 609 keV peak for ^{214}Bi, 911 keV peak for ^{228}Ac, and 1460 keV peak for ^{40}K. None of the observed background anomalies occurred in these regions. Consistency improves as the energy level increases. This is due to a decrease in continuum and coincidence summing effects. Figures 8-12 show the background net peak areas at each of these peak energies over time +/- 2σ. One outlier was observed in the 609 keV peak for ^{214}Bi during the 19 September background measurement.
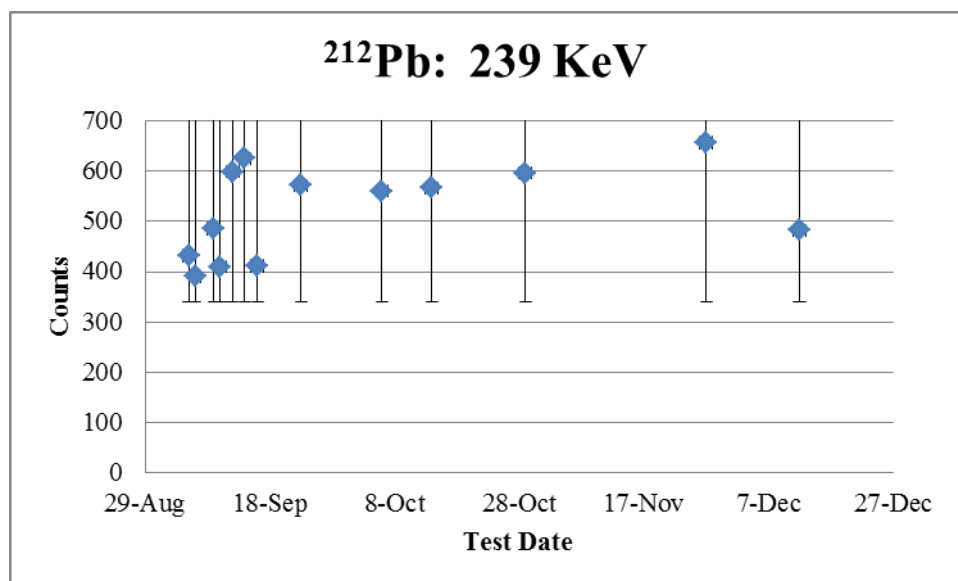
Figure 8: 239 keV Net Peak Area Over Time (+/- 2σ)
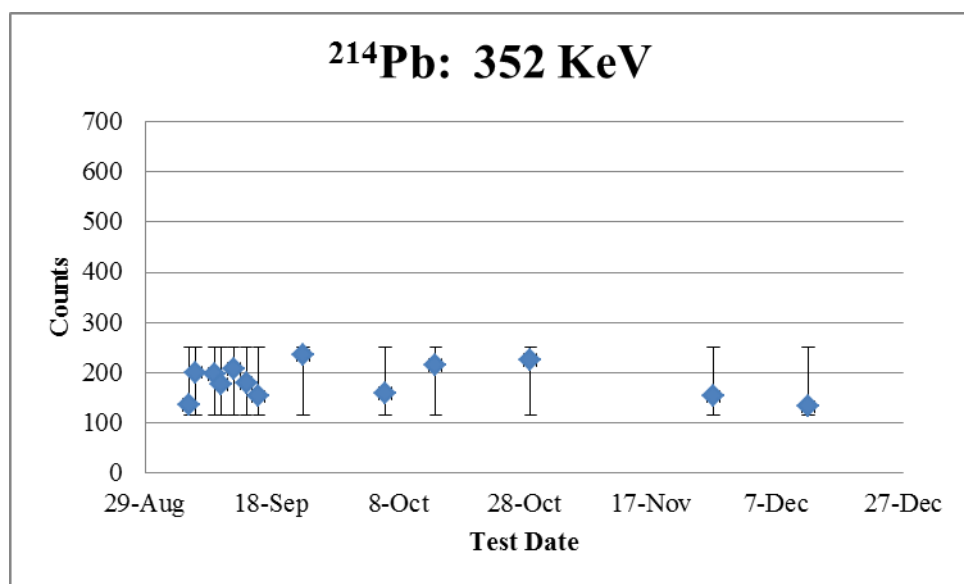
Figure 9: 352 keV Net Peak Area Over Time (+/- 2σ)

31
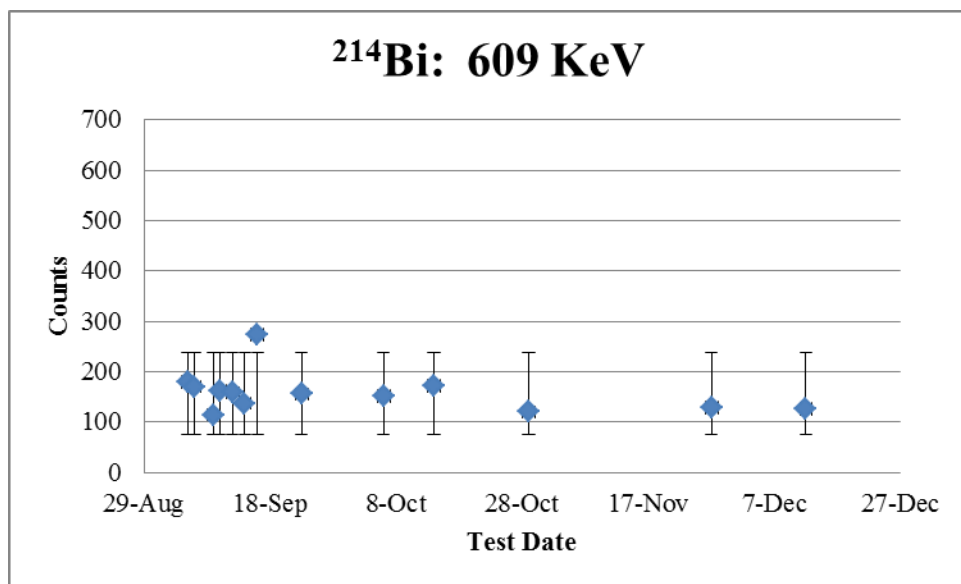
Figure 10: 609 keV Net Peak Area Over Time (+/- 2σ)
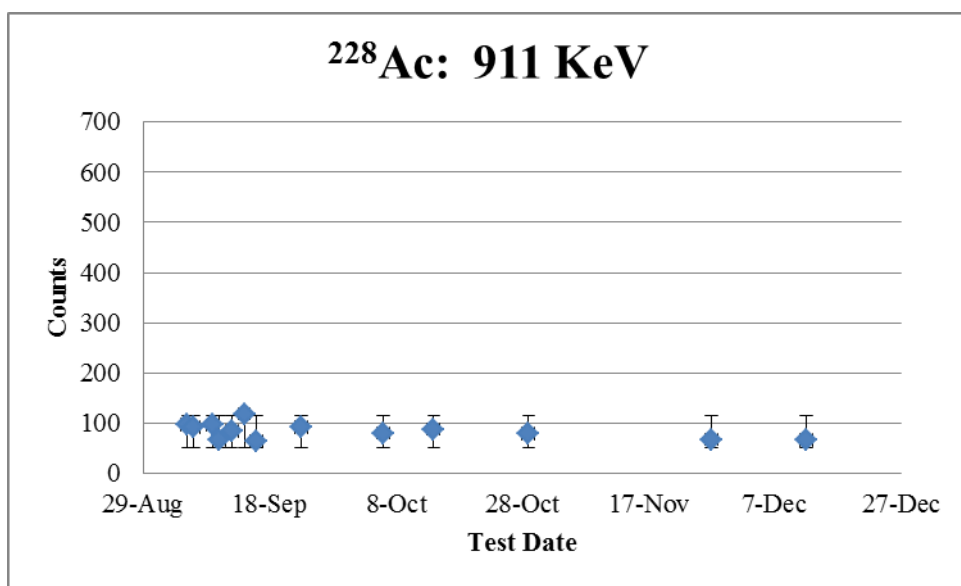
Figure 11: 911 keV Net Peak Area Over Time (+/- 2σ)
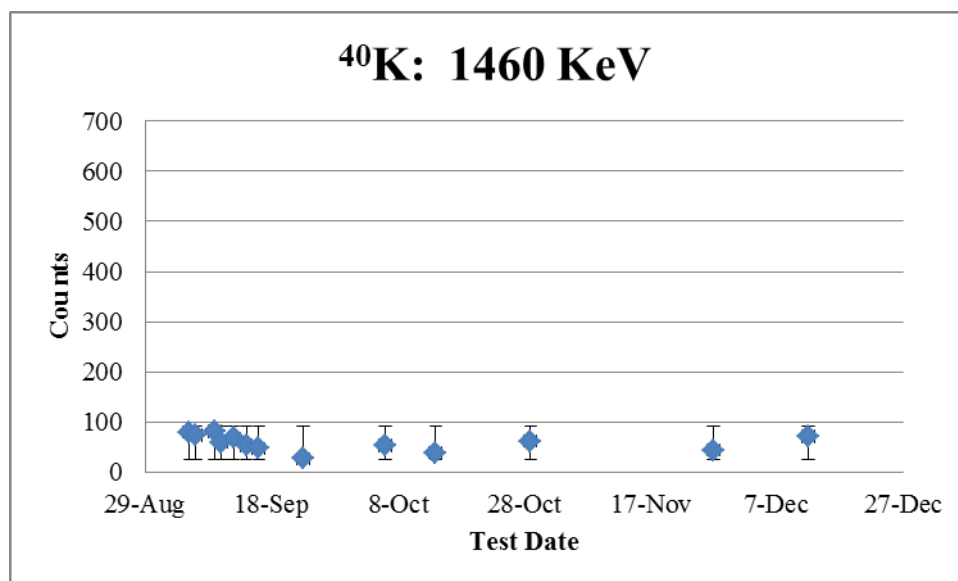
Figure 12: 1460 keV Net Peak Area Over Time (+/- 2σ)

In addition to these regions of interest and the anomaly regions, significant background peaks occur at 64 keV, 186 keV, 511 keV, and 662 keV. The 511 keV peak is the pair production single escape peak. The 662 keV peak is most likely caused by ^{137}Cs calibration standards stored in the lab. The 64 keV peak may be a result of [210]Pb b-decay from the lead materials comprising the cave and collimator. Naturally occurring [226]Ra is the most likely source of the 186 keV peak.

Material Analysis

As discussed in Chapter 3, the focus of the material sample analysis was specific to peaks produced by potassium and progeny of uranium and thorium series. For each material sample, five measurements were collected for 86,400 seconds per measurement. The resulting spectra were analyzed using the blind peak search function in GammaVision®. For each material, a weighted best value peak area was calculated for each peak of interest from the results of the five tests. The weighted best value

calculation is based on the assumption that the net peak area x is drawn from a Poisson

distribution and the mean $\bar{x} = x$. Based on this assumption $\sqrt{s^2} \cong \sigma = \sqrt{\bar{x}} = \sqrt{x}$. The

best value x_e can then be calculated for a set of measurements with unequal errors using

Equation (1) using a weighting factor calculated by Equation (2) (Knoll, 2010). The

resulting weighted best value peak areas are shown in Table 6.

$$x_e = \frac{\sum_{i=1}^{N} a_i x_i}{\sum_{i=1}^{N} a_i} \qquad (2)$$

Where:
x_e = Calculated best value
x_i = Observed net peak area
a_i = Weighting factor based on the error associated with x_i

$$a_j = \frac{1}{\sigma_{xj}^2} \left(\sum_{i=1}^{N} \frac{1}{\sigma_{xi}^2} \right)^{-1} \qquad (3)$$

Where:
a_j = Calculated weighting factor
σ_{xj}^2 = Error associated with observation j
σ_{xi}^2 = Error associated with each observation i

Table 6: Weighted Best Value Net Peak Areas

	^{214}Pb (352 keV)		^{214}Bi (609 keV)		^{212}Pb (239 keV)		^{228}Ac (911 keV)		^{40}K (1460 keV)	
	Counts	+/- 2σ	Counts	+/- 2σ	Counts	+/- 2σ	Counts	+/- 2σ	Counts	+/- 2σ
A36 Steel	140.53	38.05	163.87	29.5	574.92	50.57	73.59	15.75	37.52	11.42
Stainless Steel	197.33	31.4	137.4	22.06	441.15	46.94	90.31	21.22	49.93	11.7
Asphalt	703.24	45.34	570.34	32.34	1119.33	66.94	142.69	25.84	584.73	24.12
Sandstone	2255.09	80.46	2099.98	58.46	6788.73	135.54	1124.19	49.12	2458.92	47.99
CMU #1	946.65	42.21	516.19	30.95	1190.41	67.65	180.64	30.95	590.74	24.21
CMU#2	1152.31	52.36	906.24	38.35	1774.75	62.53	249.74	38.35	999.51	30.41
Red Brick #2	1470.06	76.38	1175.76	59.43	4758.08	110.94	807.14	37.53	2889.07	50.65
Red Brick #3	1769.92	70.85	1429.35	52.89	4443.33	110.88	714.37	36.58	2333.86	46.54
Red Brick #4	1619.51	68.39	1212.53	48.92	3962.07	112.08	671.41	44.64	3982.51	59.06
Concrete #1	761.01	45.81	575.28	33.06	1302.31	70.22	208.04	26.11	580.72	23.95
Concrete #2	640.75	44.01	525.19	31.41	1068.75	67.85	155.98	26	564.18	24.03
Concrete #3	676.29	44.38	571.2	32.53	1196.33	68.99	141.09	26.43	566.92	24.02
Concrete #4	671.08	44.91	557.44	32.02	1192.28	68.43	169.41	32.02	588.54	24.24

For each peak of interest, the best value peak areas for A36 and stainless steel fall within the range of peak areas observed in the background measurements. The steel samples do not appear to contribute to the count rate and actually provided additional shielding for the detector. The count rates observed from the asphalt concrete are similar to those observed in Portland concrete in each peak. This indicates that the binder or paste of the concrete material contributes little natural radiation and that the aggregate and sand fractions are the primary contributors.   Since the asphalt and Portland concrete were likely produced using locally quarried sand and aggregate, it would follow that they would produce similar amounts of natural radiation. This analysis can be carried over to the CMU samples. CMU #1 was provided by a local brick and block producer. The peak areas show that, with the exception of elevated counts from ^{214}Pb, CMU #1 had similar natural radioactivity to Portland concrete. CMU #2, however, was provided by a big box building supply store. Net peak areas were higher for every region of interest for this material. The net peak area of the clay brick products was higher than any of the

concrete products for each region of interest. Only the sandstone block exceeded the

natural radioactivity of the clay bricks.

4.2 Results of X-ray Fluorescence

The X-ray fluorescence experiments produced spectral data and quantitative

analysis results.   Spectral data, similar to the gamma spectroscopy output, contained a

number of successful counts for each channel. The Horiba software allows the user to

perform quantitative analysis on the spectral data to identify elements and estimate

quantities. In this case, the fundamental principles method was used to estimate

quantities of oxides by percentage of sample mass. The Horiba XGT-7000 was pre-

calibrated for energy and efficiency. Discrepancies in the data could be caused by

sample preparation method, instrument properties, and software limitations. Areas of

concern for quantitative data accuracy are listed below.

1. Contamination of sample powders from preparation process.
2. Sample particle size inconsistency.
3. Influence of instrument rhodium target.
4. Accuracy of trace element peak identification.

The sample powders were prepared using a high speed steel masonry drill bit.

High speed tool steel chemical composition standards are described in AST A600-92a.

There are two primary categories of high speed steel alloys, tungsten and molybdenum.

For the various grades of tungsten tool steel, tungsten content requirements range from

13.25% to 21%. For the various grades of molybdenum type tool steel, molybdenum

content requirements range from 3.25% to 11% (ASTM, 2004). Tungsten was not

identified in any of the quantitative results. Trace amounts of Molybdenum were

identified in Concrete #1 and Concrete#2. For Concrete #1, a trace amount of

molybdenum was identified at test point 2 of 12. For Concrete #2, a trace amount of

molybdenum was identified at test point 7 of 12. The results do not indicate a pattern for

tool steel contamination. The spectral plots for these data points with the molybdenum

characteristic X-ray signature for reference are shown in Figure 13.
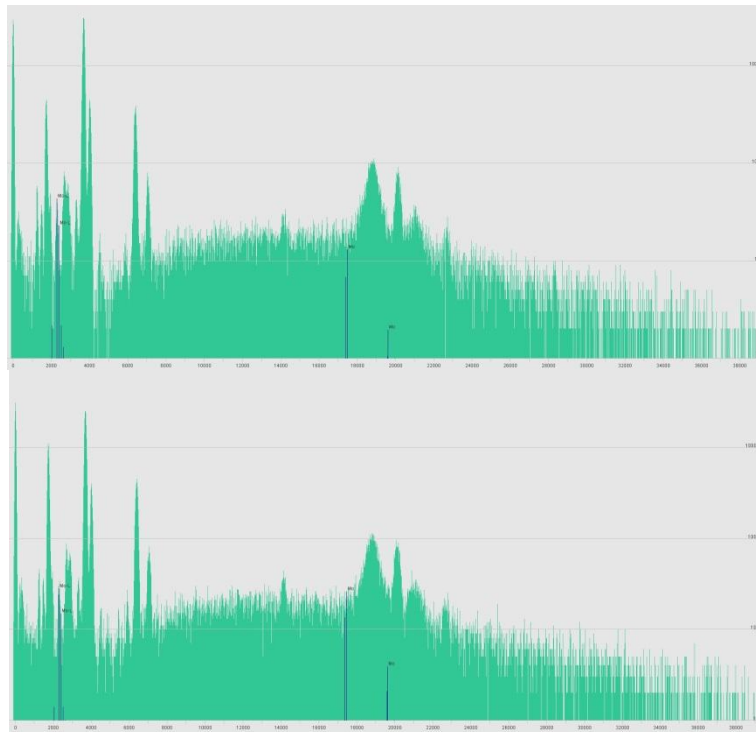
**Figure 13: XRF Spectral Plots (log) for Concrete #1 Point 3 (top) and Concrete #2
Point 7 (bottom) with Mo X-ray signatures (blue lines)**

Particle size inconsistency could cause large variations in spectral and quantitative results for test points within a sample. The experiments were conducted using the 100 micrometer X-ray beam over 12 points for each sample to reduce the influence of large particles on the results. The range for the quantitative results from the 12 test points was reported to show the possibility of large particle influence.

The Horiba XGT-7000 contains a rhodium target. The rhodium signature from this target is present in all of the spectral and quantitative results. This signature is produced by the Kα1 X-ray at 20.216 keV, Kα2 X-ray at 20.074 keV, Kβ1 X-ray at 22.724 keV, and Kβ3 X-ray at 22.699 (Kotright & Anderson, 2009). These X-ray peaks also produce visible continuums. The rhodium target signature is shown in Figure 14. This figure shows the average of the spectra from all 12 points for each sample at the top and the rhodium x-ray lines against the spectrum produced at point one of the asphalt sample at the bottom.
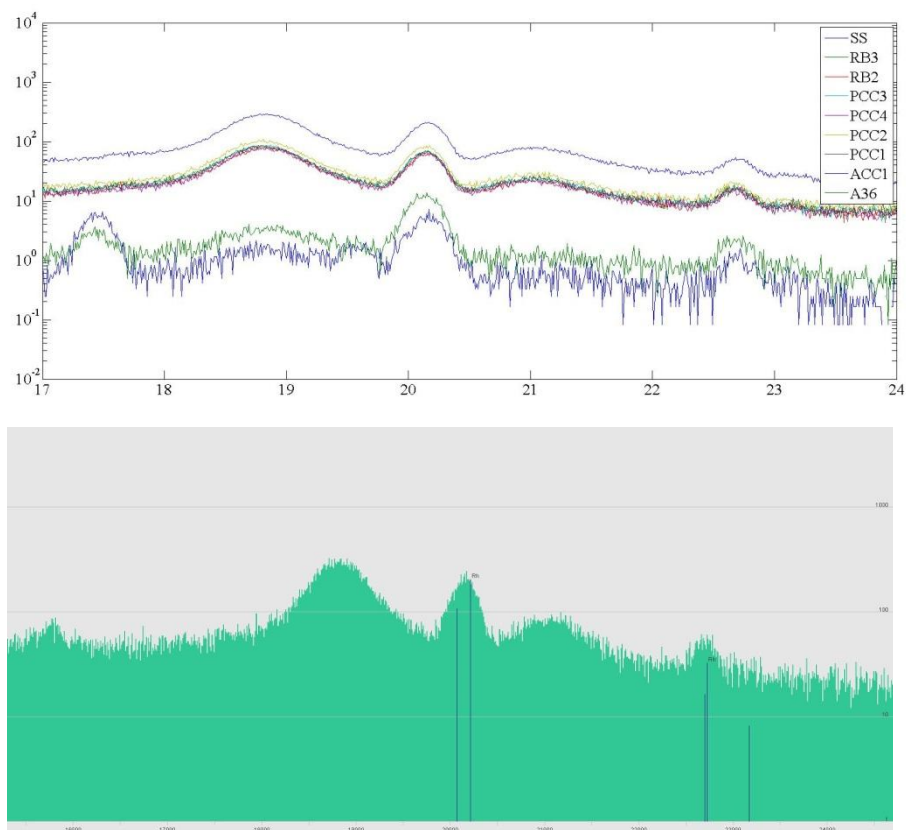
Figure 14: Rhodium Signature in XRF Spectral Plots (log) Averaged Spectra (top) and Asphalt Point 1(bottom) with Rh X-ray signatures (blue lines)

In some cases, the software identified elements and quantified them at 0.00% of the sample mass. The calculated quantities were smaller than the software's significant figure limit. This was the case with the previously discussed molybdenum identifications in the concrete samples. Another example was the identification of uranium oxide in the stainless steel sample at point 10. Uranium has an Mα1 X-ray at 3.170 keV (Kotright & Anderson, 2009).   At point 10, the quantification results also indicated the presence of nickel (7.26%) and molybdenum (0.4%). A summing peak for nickel and molybdenum occurs at 3.144 keV. In this case, the peak identified as uranium by the software is more

39

likely caused by the summing of nickel and molybdenum. The peak and reference lines

for the uranium X-ray and summed nickel- molybdenum X-ray are shown in Figure 15.
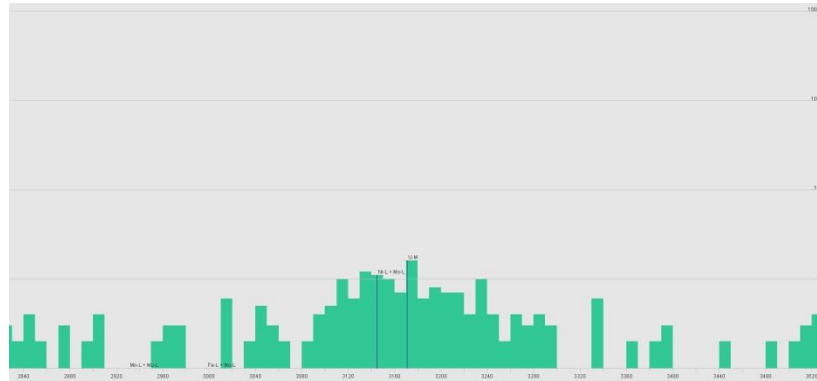
**Figure 15: Stainless Steel Point 10 XRF spectrum (log) with uranium and
summed nickel molybdenum X-rays (blue lines)**

The XRF analysis discussed below was carried out with the previously mentioned

limitations in mind. Although gamma spectroscopy results showed the steel samples

contribute very little radiation, the XRF results from these samples were helpful in

assessing the instruments performance. Chemical compositions results for the metals

samples were at or near the ASTM standards listed in Chapter II.   The measured

chemical composition for A36 steel is provided in Table 7. Figure 16 shows the spectral

plot for A36 steel at point on with X-ray identification markers. Table 8 and Figure 17

show the same data for stainless steel.

Table 7: Composition of A36 Steel (% Mass)

	Mean	Range			Standard Deviation
A36 (n=12)					
Cr2O3	0.03	0.00	-	0.11	0.05
MnO2	0.89	0.80	-	1.02	0.06
Fe2O3	97.76	97.41	-	98.17	0.27
CuO	0.14	0.00	-	0.27	0.12
Rh2O3	1.01	0.90	-	1.11	0.07
La2O3	0.16	0.00	-	0.42	0.20
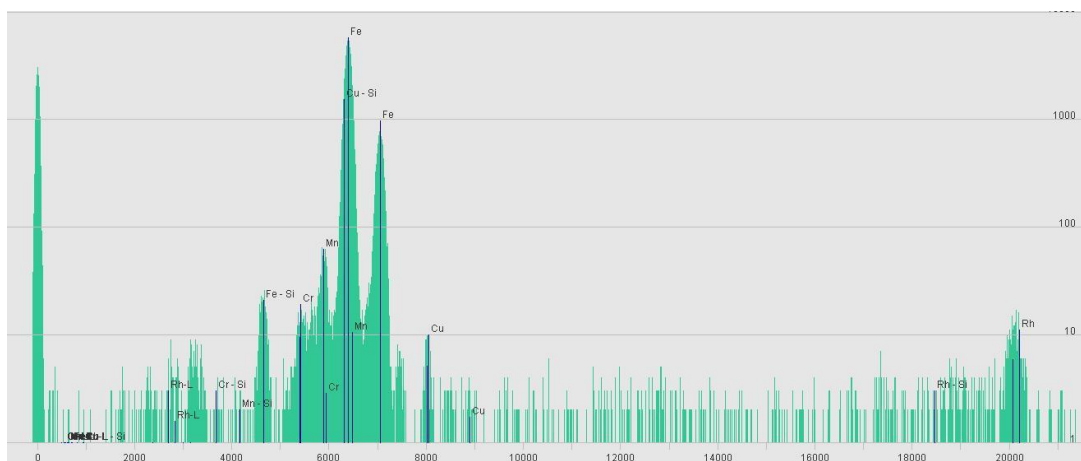
Figure 16: XRF Spectral Plots (log) A36 Steel Point 1 with X-ray signatures (blue lines)

41

Table 8: Composition of Stainless Steel (% Mass)

	Mean	Range			Standard Deviation
Stainless Steel (n=12)					
Cr2O3	18.81	17.45	-	23.25	1.50
MnO2	1.50	1.21	-	1.96	0.21
Fe2O3	71.26	67.68	-	72.82	1.43
NiO	8.00	7.11	-	8.98	0.57
MoO3	0.15	0.00	-	0.40	0.19
Rh2O3	0.09	0.00	-	1.10	0.32
Gd2O3	0.01	0.00	-	0.10	0.03
Dy2O3	0.20	0.00	-	0.33	0.16
U3O8	0.00	0.00	-	0.00	0.00
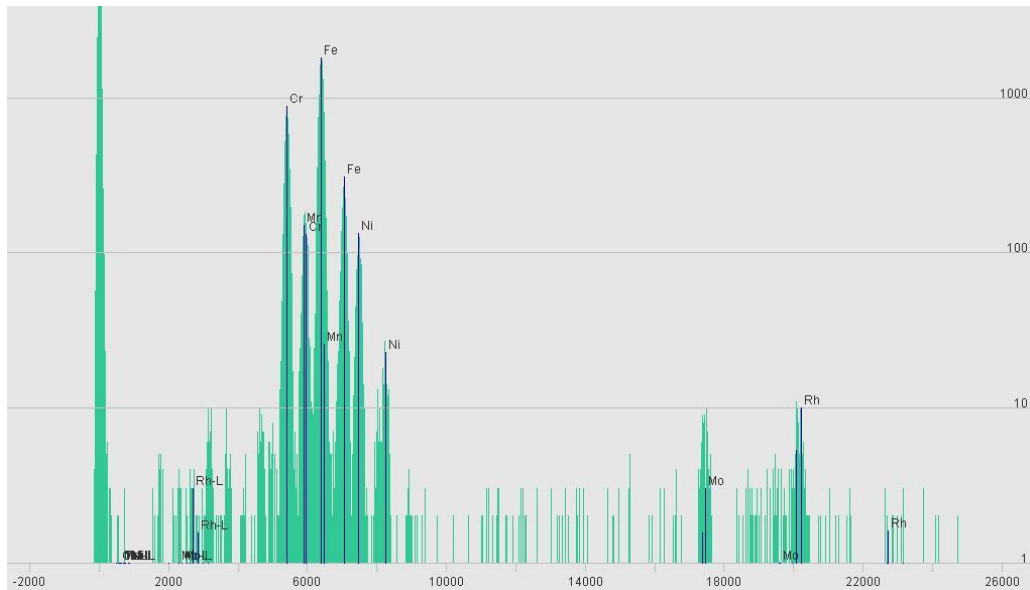
Figure 17: XRF Spectral Plots (log) Stainless Steel Point 10 with X-ray signatures (blue lines)

42

Asphalt was the most chemically complex material sampled.   The largest fraction of the material mass consisted of silicon and calcium. This was expected due to calcium carbonate aggregates and silica sand in the asphalt mix. Asphalt concrete should be similar to Portland concrete aside from the binder material. The petroleum based asphalt consists of hydrocarbons which are not detectable by XRF. A large number of trace metals appeared in the quantification results. These trace elements include chromium, nickel, scandium, palladium, and mercury. The palladium result is most likely an artifact from instrument components. Asphalt binders are known to contain trace amounts of vanadium and nickel (Jones, 1993).   Waste engine oil is sometimes used to produce asphalt binders and is known to contain chromium and zinc. However, lead is typically present at higher concentrations than chromium or zinc in waste oil (Rauckyte, Hargreaves, & Pawlak, 2006). Asphalt composition results are shown in Table 9, and a typical spectrum is shown in Figure 18.

Table 9: Composition of Asphalt (% Mass)

	Mean	Range			Standard Deviation
Asphalt (n=12)					
MgO	9.93	4.69	-	12.79	3.08
Al_2O_3	2.79	0.98	-	8.03	1.98
SiO_2	35.92	10.91	-	70.27	18.87
SO_3	1.11	0.53	-	1.75	0.35
K_2O	0.98	0.15	-	7.14	1.95
CaO	44.00	18.32	-	67.67	14.41
Sc_2O_3	0.10	0.00	-	1.20	0.35
TiO_2	0.34	0.11	-	1.11	0.32
V_2O_5	0.01	0.00	-	0.14	0.04
Cr_2O_3	0.01	0.00	-	0.13	0.04
MnO_2	0.12	0.00	-	0.28	0.09
Fe_2O_3	3.33	1.00	-	5.66	1.47
NiO	0.01	0.00	-	0.08	0.02
Rb_2O	0.00	0.00	-	0.01	0.00
ZnO	0.01	0.00	-	0.06	0.02
SrO	0.06	0.02	-	0.09	0.02
ZrO_2	0.09	0.00	-	0.65	0.20
Rh_2O_3	1.04	0.63	-	1.46	0.26
PdO	0.04	0.00	-	0.20	0.07
TeO_2	0.01	0.00	-	0.07	0.02
Ta_2O_5	0.06	0.00	-	0.68	0.20
Re_2O_7	0.02	0.00	-	0.18	0.05
Ir_2O_3	0.00	0.00	-	0.00	0.00
HgO	0.02	0.00	-	0.21	0.06
Ac_2O_3	0.00	0.00	-	0.04	0.01
Eu_2O_3	0.05	0.00	-	0.59	0.17
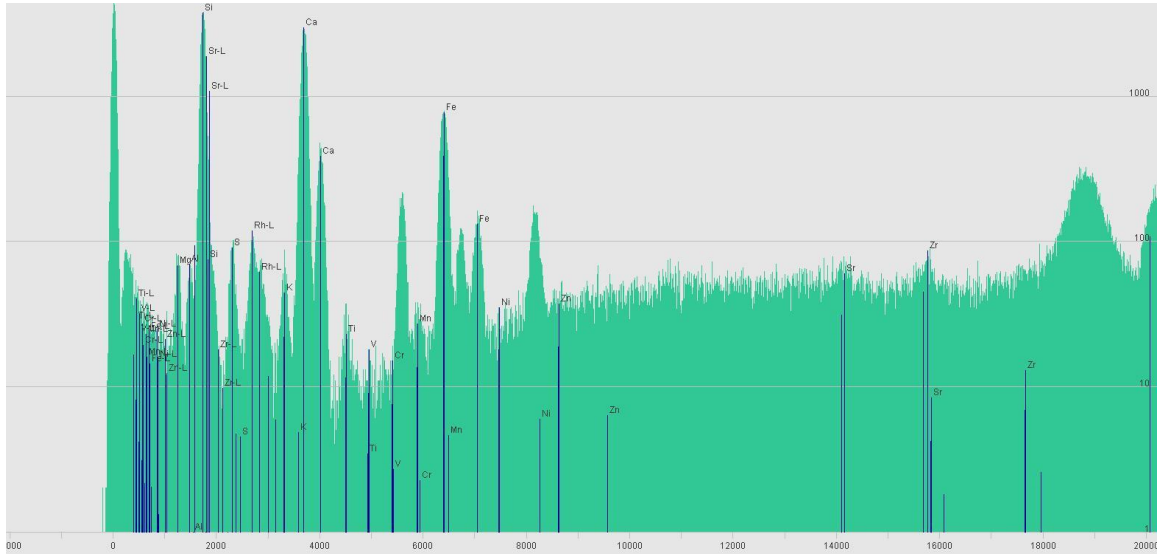
Figure 18: XRF Spectral Plots (log) Asphalt Concrete 1 with X-ray signatures (blue lines)

The primary components of the sandstone brick were silicon, aluminum,

potassium, iron, and titanium. These results are consistent with the expectation that the

material is composed of silica sand. The composition of the sandstone sample is shown

in Table 10 and the XRF spectrum is shown in Figure 19.

Table 10: Composition of Sandstone (% Mass)

	Mean	Range			Standard Deviation
Sandstone (n=12)					
Al_2O_3	21.64	18.04	-	25.38	1.97
SiO_2	67.98	64.76	-	73.24	2.32
SO_3	0.08	0.00	-	0.54	0.16
K_2O	3.21	2.66	-	3.96	0.40
CaO	0.49	0.31	-	0.76	0.13
TiO_2	2.44	2.06	-	3.03	0.29
Cr_2O_3	0.01	0.00	-	0.07	0.02
MnO_2	0.33	0.00	-	3.90	1.12
Fe_2O_3	2.94	0.03	-	3.98	0.99
Rb_2O	0.04	0.02	-	0.12	0.03
SrO	0.15	0.05	-	0.86	0.23
ZrO_2	0.18	0.07	-	0.77	0.19
Rh_2O_3	0.57	0.49	-	0.67	0.05
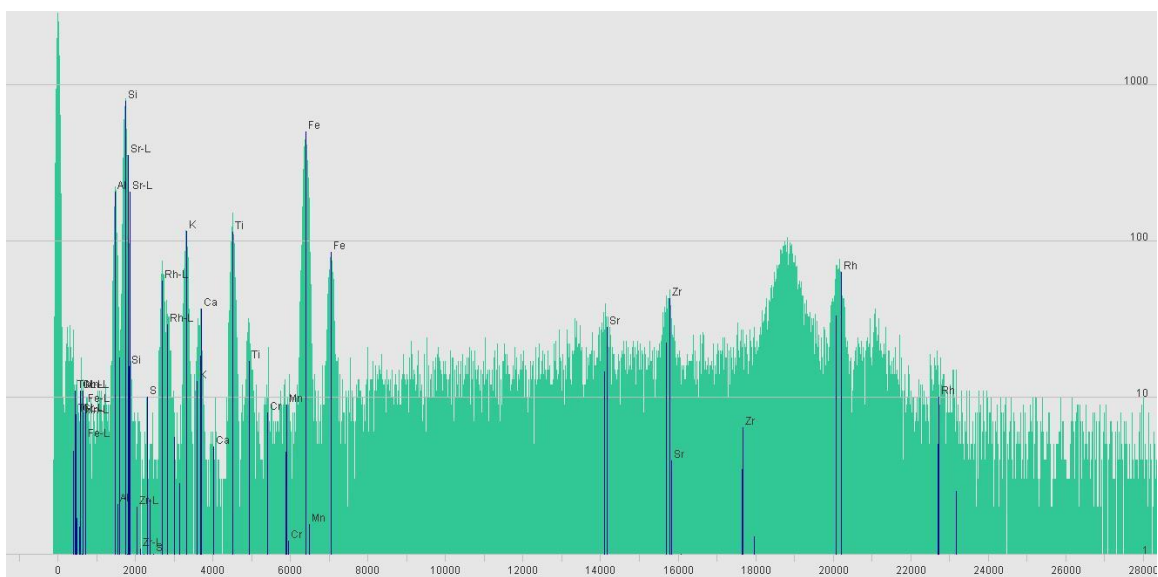
Figure 19: XRF Spectral Plots (log) Sandstone Point 5 with X-ray signatures (blue lines)

Components of the red brick samples, in order of decreasing concentration, were silicone, aluminum, iron, potassium, and titanium. Magnesium made up 5.6% of red brick #4. Magnesium was unique to this sample. In contrast to asphalt and Portland concrete, the red brick samples contained less than 1% calcium by mass. Red brick compositions are shown in Tables 11 to 13. A spectrum from red brick #2 is provided as an example in Figure 20.

Table 11: Composition of Red Brick (% Mass)

	Mean	Range			Standard Deviation
Red Brick #2					
(n=12)					
Al_2O_3	20.49	14.58	-	30.25	5.01
SiO_2	60.76	49.94	-	71.06	6.10
K_2O	3.51	2.44	-	3.89	0.43
CaO	0.02	0.00	-	0.24	0.07
TiO2	1.38	1.16	-	1.85	0.21
Cr_2O_3	0.01	0.00	-	0.06	0.02
MnO_2	0.12	0.08	-	0.27	0.05
Fe_2O_3	12.90	9.10	-	16.16	1.62
CuO	0.00	0.00	-	0.03	0.01
Rb_2O	0.02	0.00	-	0.04	0.02
SrO	0.01	0.00	-	0.04	0.02
ZrO_2	0.05	0.04	-	0.07	0.01
Nb_2O_5	0.00	0.00	-	0.02	0.01
Rh_2O_3	0.70	0.58	-	0.98	0.11
PdO	0.03	0.00	-	0.23	0.07

Table 12: Composition of Red Brick (% Mass)

	Mean	Range			Standard Deviation
Red Brick #3 (n=12)					
Al_2O_3	18.71	14.90	-	26.77	3.79
SiO_2	61.14	52.83	-	67.04	4.97
K_2O	2.89	2.38	-	3.21	0.23
CaO	0.98	0.72	-	1.25	0.17
TiO_2	1.53	1.02	-	3.49	0.70
V_2O_5	0.04	0.00	-	0.50	0.14
MnO_2	0.21	0.18	-	0.29	0.03
Fe_2O_3	13.68	12.14	-	20.53	2.24
ZnO	0.01	0.00	-	0.05	0.02
Rb_2O	0.03	0.00	-	0.04	0.01
SrO	0.03	0.00	-	0.05	0.02
ZrO_2	0.06	0.03	-	0.12	0.02
Rh_2O_3	0.70	0.60	-	0.78	0.05

Table 13: Composition of Red Brick (% Mass)

	Mean	Range			Standard Deviation
Red Brick #4 (n=12)					
MgO	5.62	5.62	-	5.62	1.62
Al_2O_3	24.72	17.40	-	27.68	2.48
SiO_2	54.73	51.60	-	57.86	1.98
K_2O	5.21	4.83	-	5.93	0.33
CaO	0.52	0.00	-	0.83	0.20
TiO_2	1.42	1.12	-	1.67	0.16
Cr_2O_3	0.01	0.00	-	0.07	0.02
MnO_2	0.13	0.09	-	0.19	0.03
Fe_2O_3	11.91	10.69	-	13.48	0.98
CuO	0.00	0.00	-	0.05	0.01
ZnO	0.03	0.00	-	0.10	0.03
Rb_2O	0.04	0.03	-	0.06	0.01
ZrO_2	0.06	0.04	-	0.10	0.02

| Rh$_2$O$_3$ | 0.74 | 0.58 - 0.88 | 0.08 |
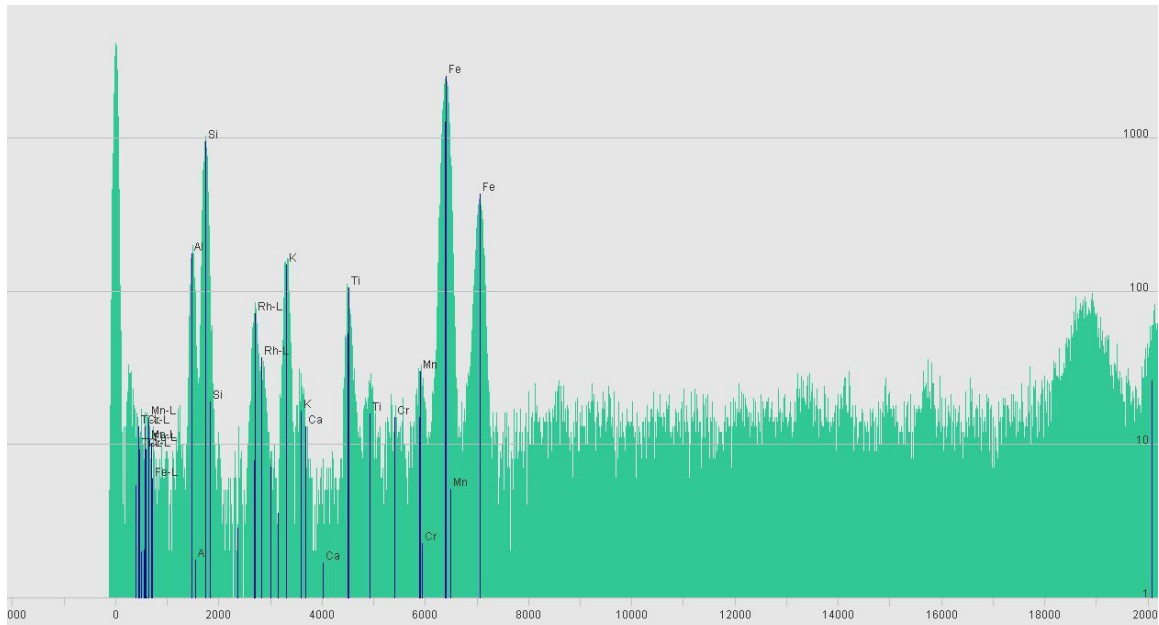
Figure 20: XRF Spectral Plots (log) Red Brick #2 Point 1 with X-ray signatures (blue lines)

Components of the Portland concrete samples, in order of decreasing concentration, included calcium, silicone, magnesium, aluminum, and iron. Sulphur, chlorine, potassium, and manganese were also present in the samples. Portland concrete compositions are shown in Tables 14 to 17. A spectrum from Portland concrete sample #2 is provided as an example in Figure 21.

Table 14: Composition of Portland Concrete (% Mass)

	Mean	Range			Standard Deviation
Concrete #1 (n=12)					
MgO	12.43	5.31	-	16.34	3.06
Al_2O_3	2.81	1.88	-	5.84	1.21
SiO_2	28.01	21.16	-	40.83	5.74
SO_3	0.61	0.00	-	0.98	0.23
Cl	0.08	0.00	-	0.26	0.12
K_2O	0.63	0.30	-	1.04	0.25
CaO	50.37	43.11	-	54.57	3.60
TiO_2	0.09	0.00	-	0.46	0.15
MnO_2	0.07	0.00	-	0.19	0.07
Fe_2O_3	3.68	2.10	-	6.10	1.31
SrO	0.04	0.00	-	0.10	0.03
ZrO_2	0.04	0.00	-	0.44	0.13
MoO_3	0.00	0.00	-	0.00	0.00
Rh_2O_3	1.13	1.02	-	1.39	0.11
PdO	0.01	0.00	-	0.16	0.05
SnO_2	0.00	0.00	-	0.00	0.00
SrO	0.06	0.00	-	0.12	0.03
ZrO_2	0.01	0.00	-	0.07	0.02
Rh_2O_3	1.09	0.85	-	1.28	0.13
SnO_2	0.00	0.00	-	0.01	0.00

Table 15: Composition of Portland Concrete (% Mass)

	Mean	Range			Standard Deviation
Concrete #2					
(n=12)					
MgO	10.83	7.85	-	13.67	1.64
Al_2O_3	2.89	0.00	-	4.66	1.21
SiO_2	31.36	17.35	-	51.60	11.25
SO_3	0.65	0.00	-	1.02	0.28
Ar	0.02	0.00	-	0.18	0.05
K_2O	0.43	0.00	-	0.68	0.18
CaO	47.72	33.82	-	62.29	9.10
TiO_2	0.43	0.00	-	2.13	0.57
Cr_2O_3	0.01	0.00	-	0.07	0.02
MnO_2	0.09	0.00	-	0.33	0.11
Fe_2O_3	4.38	1.94	-	7.09	1.73
Br_2O	0.00	0.00	-	0.00	0.00
SrO	0.08	0.06	-	0.12	0.02
MoO_3	0.00	0.00	-	0.00	0.00
Rh_2O_3	1.11	0.87	-	1.35	0.16
In_2O_3	0.00	0.00	-	0.00	0.00
SnO_2	0.00	0.00	-	0.01	0.00
Ac_2O_3	0.00	0.00	-	0.02	0.01
ThO_2	0.00	0.00	-	0.00	0.00

Table 16: Composition of Portland Concrete (% Mass)

	Mean	Range			Standard Deviation
Concrete #3 (n=12)					
MgO	10.06	6.85	-	15.66	2.42
Al_2O_3	2.87	2.10	-	4.68	0.70
SiO_2	26.54	18.30	-	43.75	7.81
SO_3	1.21	0.48	-	2.04	0.44
K_2O	0.73	0.36	-	1.43	0.33
CaO	52.03	33.98	-	60.95	8.46
TiO_2	0.24	0.00	-	0.57	0.18
MnO_2	0.15	0.00	-	0.73	0.20
Fe_2O_3	5.03	1.26	-	22.05	5.48
SrO	0.06	0.00	-	0.12	0.03
ZrO_2	0.01	0.00	-	0.07	0.02
Rh_2O_3	1.09	0.85	-	1.28	0.13
SnO_2	0.00	0.00	-	0.01	0.00

Table 17: Composition of Portland Concrete (% Mass)

|	Mean	Range			Standard Deviation
Concrete #4 *(n=12)*					
MgO	9.62	6.99	-	14.11	2.04
Al_2O_3	3.12	2.29	-	4.27	0.77
SiO_2	28.26	19.24	-	50.21	8.91
P_2O_5	0.11	0.00	-	1.31	0.38
SO_3	0.83	0.39	-	1.35	0.28
Cl	0.13	0.00	-	0.27	0.12
K_2O	0.67	0.00	-	1.45	0.43
CaO	51.96	38.97	-	61.44	6.95
TiO_2	0.08	0.00	-	0.28	0.12
MnO_2	0.32	0.00	-	2.60	0.76
Fe_2O_3	4.18	1.77	-	14.71	3.48
ZnO	0.01	0.00	-	0.08	0.02
SrO	0.08	0.05	-	0.11	0.02
Rh_2O_3	1.16	1.02	-	1.35	0.09
PdO	0.01	0.00	-	0.08	0.03
SnO_2	0.01	0.00	-	0.06	0.02
Ir_2O_3	0.00	0.00	-	0.02	0.01
PbO	0.00	0.00	-	0.00	0.00
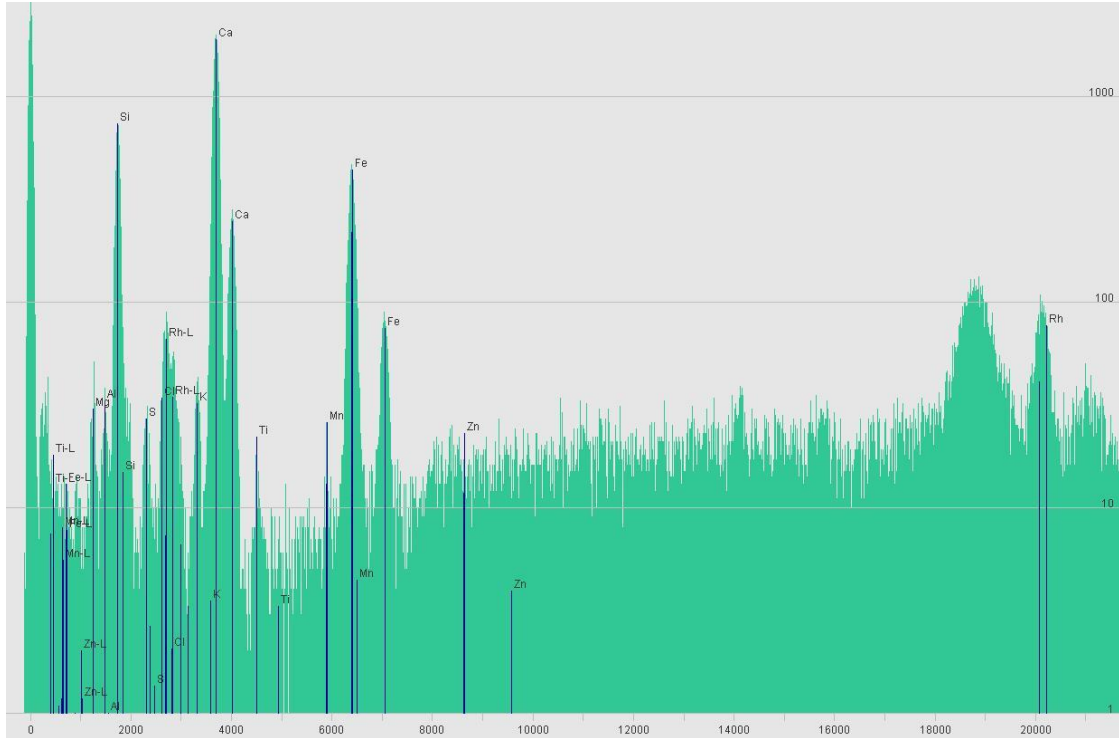
Figure 21: XRF Spectral Plots (log) Portland Concrete #2 Point 1 with X-ray signatures (blue lines)

4.3 Results of Hyper-spectral Imaging

The hyper-spectral data from the five tests at three points were averaged to produce the signature plot for each material. The averaged plot was then analyzed qualitatively to characterize material features. Discontinuities appeared in the plots at 750 nm and 1830 nm. The ASD FieldSpec 3 uses three internal sensors. The discontinuities are instrument artifacts which occur at the boundaries of the sensors' range.

The sandstone sample exhibited the highest reflectance in relation to the reference white. The distinguishing features include a strong absorption at 1900 nm and a strong peak at 2140 nm. Additional absorptions occurred at 880 nm, 1400 nm, and 2200 nm. Peaks also appeared at 760 nm and 2360 nm with peak shoulders at 615 nm and 2300 nm. The hyper-spectral plot for sandstone is shown in Figure 22. Absorption bands at 1400 and 1900 nm indicate the presence of water (Clark, 1999).
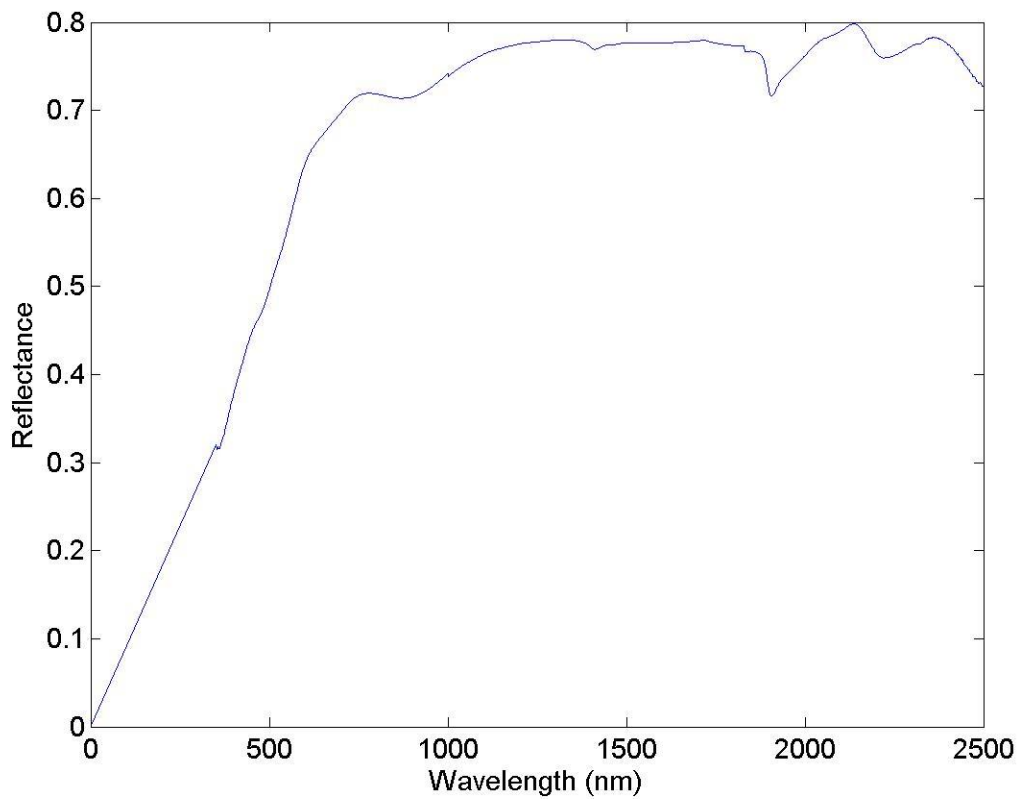

Figure 22: Sandstone Hyper-spectral Plot

The hyper-spectral plots for the red brick samples showed peaks at 770 nm and 2140 nm. Absorptions appear in all three samples at 880 nm and 2200 nm. Red Brick #4 showed absorption at 1900 nm. This feature is weak but visible in Red Brick #3. It is not visible in Red Brick #2. The hyper-spectral plots for the red brick samples are shown together in Figure 23.
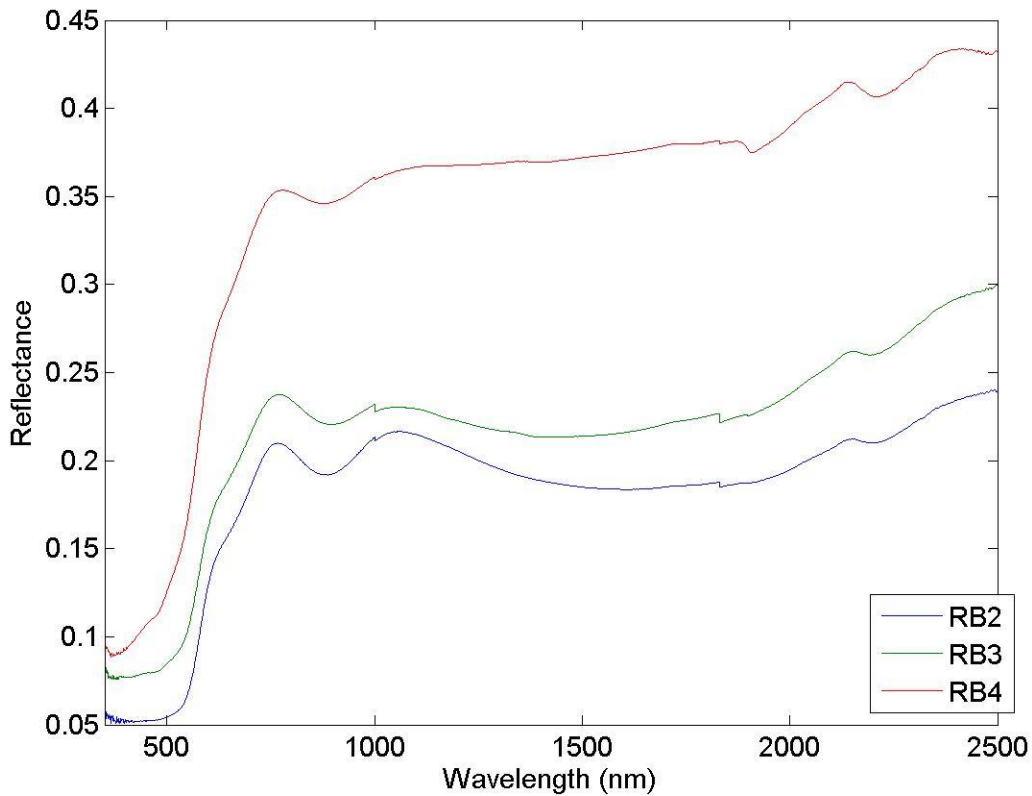

Figure 23: Red Brick Hyper-spectral Plots

All four Portland concrete samples had water absorption features at 1400 nm and 1900 nm. A strong absorption at 2330 nm appeared in all of the samples with a faint

absorption feature visible at 2200 nm. PCC #1 displayed absorption at 670 nm. This feature is faint in PCC #4 and not visible in the other two samples. All four samples had a very faint absorption at 470 nm. The hyper-spectral plots for the PCC samples are shown in Figure 24.
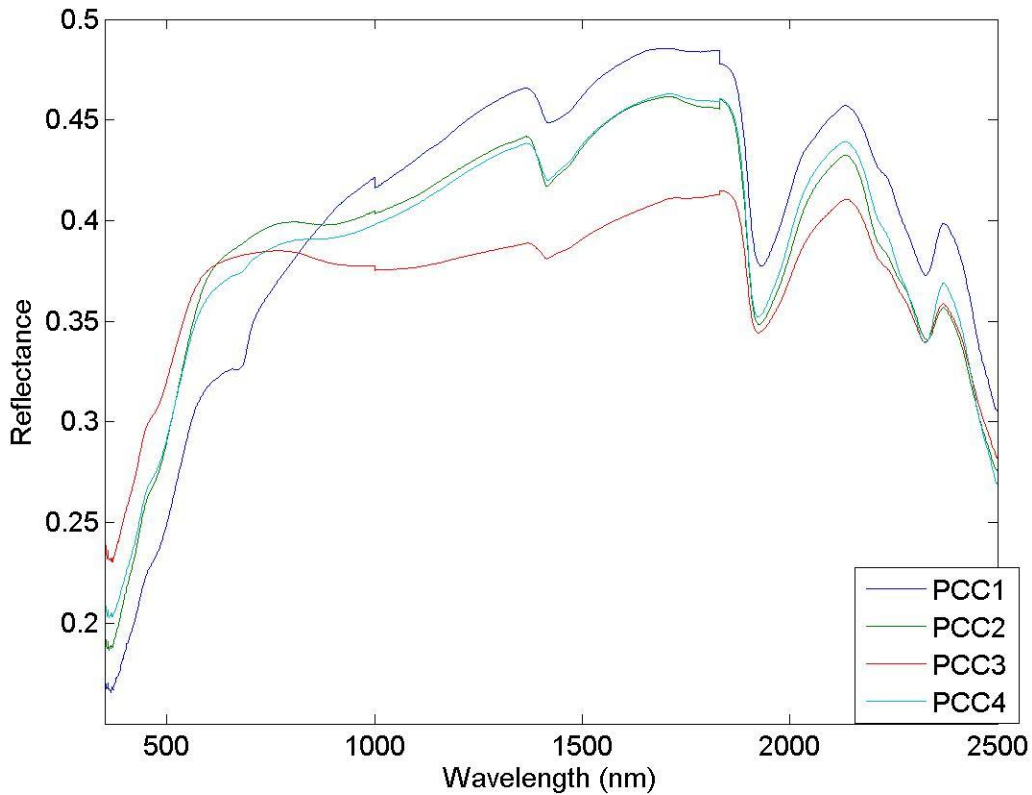

Figure 24: Portland Concrete Hyper-spectral Plots

The CMU and ACC samples show similar features to the Portland concrete samples. Stainless steel had higher reflectance than A36 steel. The structural A36 steel had a flat, featureless spectral plot. The hyper-spectral plots for the CMU, ACC, A36, and stainless steel samples are shown in Figure 25.
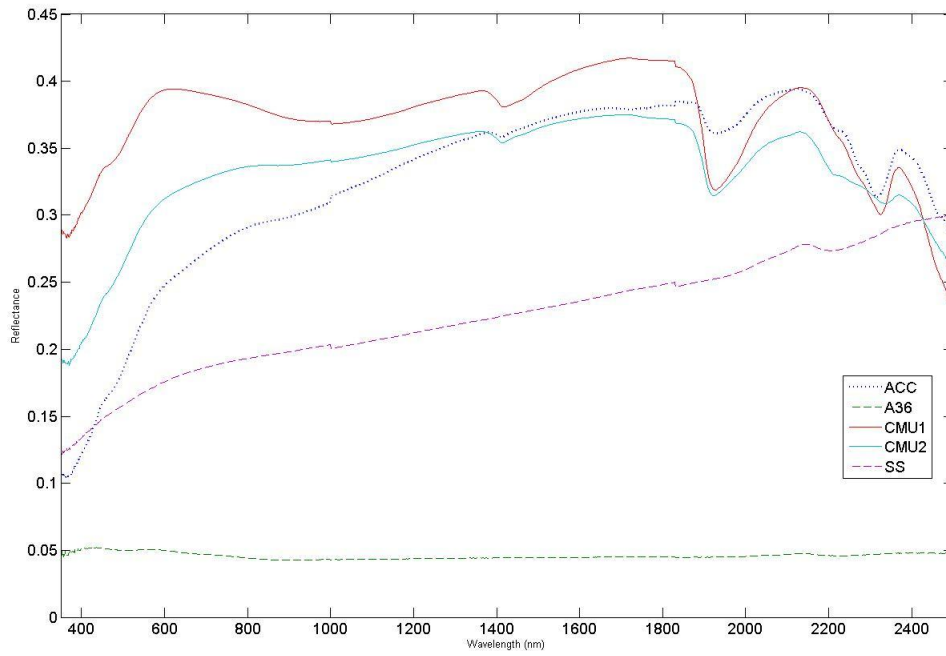
Figure 25: Hyper-spectral Plots

The spectral plots were also compared in terms of the angle between vectors as described in Chapter III. The angles between each samples spectrum are presented in the radar plots in Figure 26. A larger angle indicates a greater difference between the two samples.
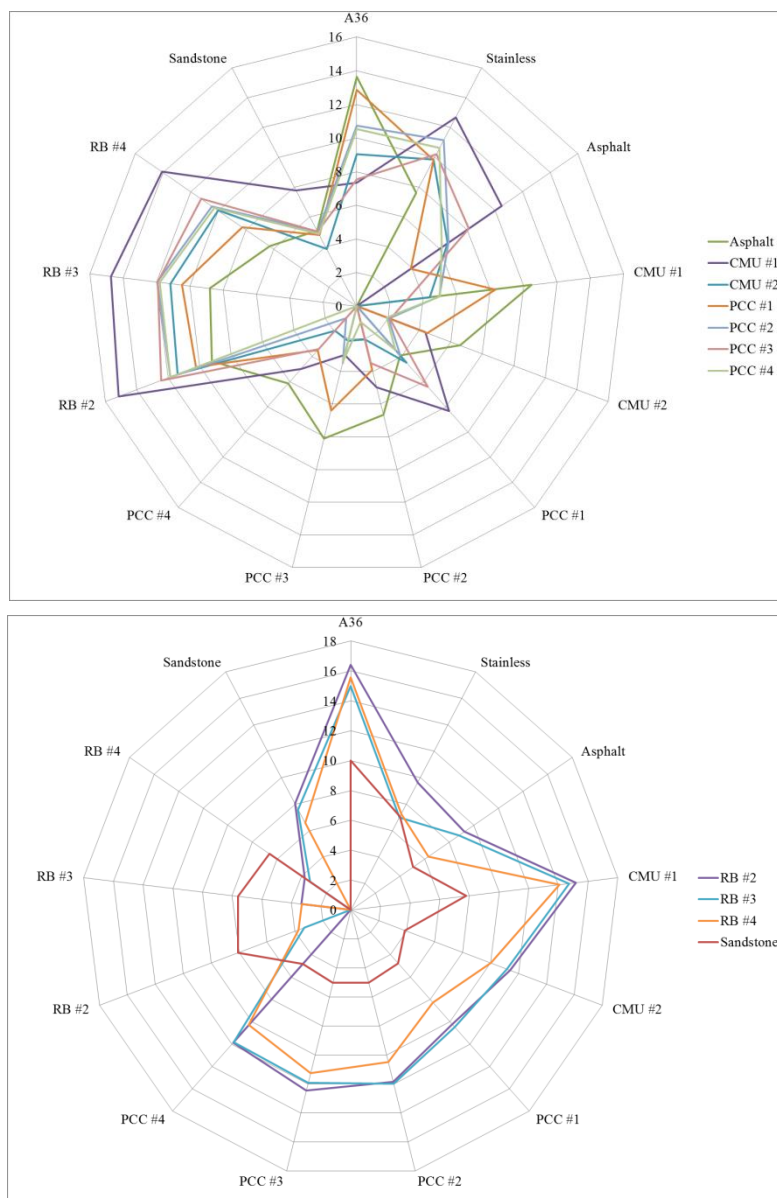
Figure 26: Radar Plots of Spectral Angle (Ө, Degrees) Between Materials. Larger Angles Indicate a Greater Difference Between the Spectral Features of Materials

Sandstone and Portland concrete had similar water absorption features. However, the two materials were distinguishable from one another by the absorption at 880 nm in sandstone and the 2330 nm absorption in PCC. The red brick samples were similar to sandstone at the 880 nm and 2200 nm absorption. However, the overall level of

reflectance was much lower in the red brick sample, and the water absorption features were faint or absent.

4.4 Overall Results

The analysis included a comparison of the content of certain compounds to net area counts in the peaks of interest. An example of this is the comparison of potassium content to 1460 keV peak counts. Materials which contain more potassium contain are more likely to contain unstable ^{40}K. As a result, ^{40}K decay will produce higher counts rates at the 1460 keV peak. Plotting the potassium content as a percentage of mass against the net peak counts at 1460 keV demonstrates that a linear relationship exists between the two sets of data as expected. This plot is shown in Figure 27.
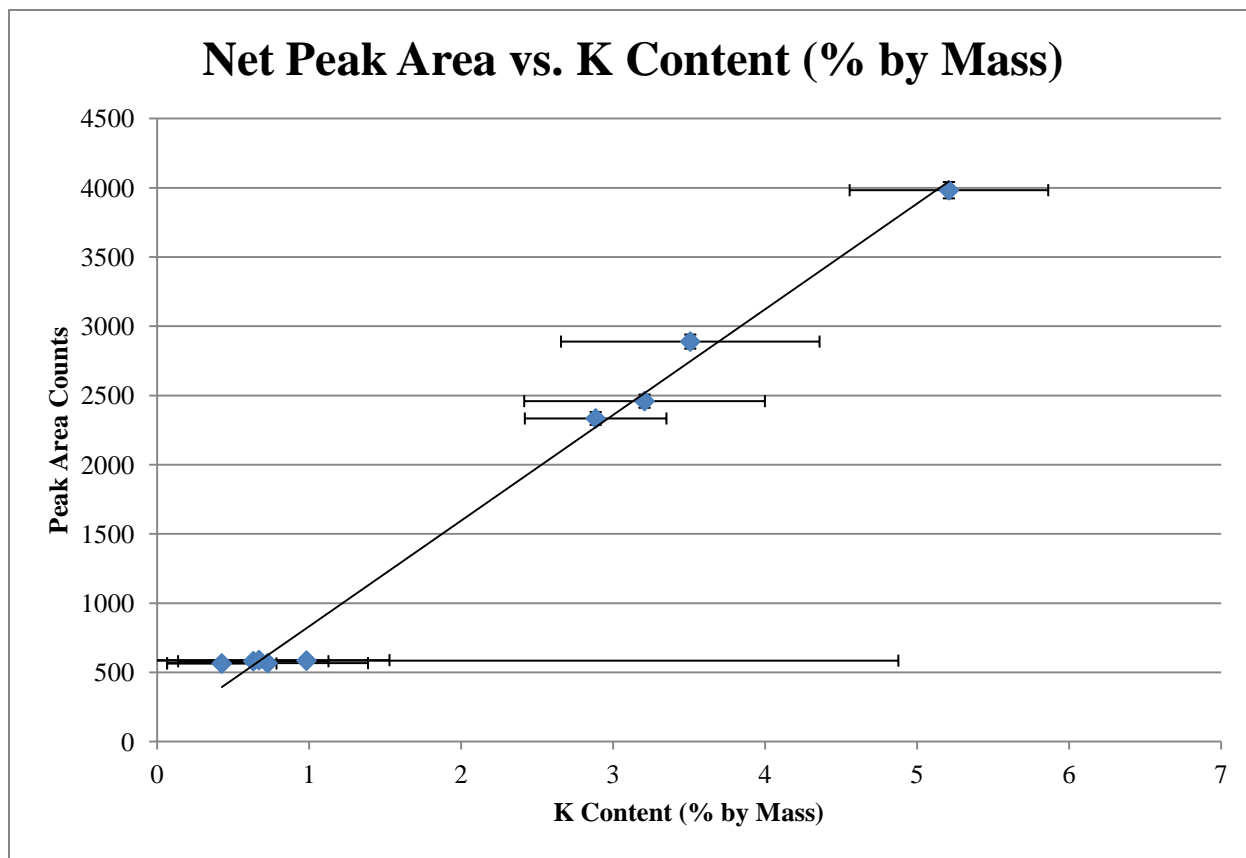
Figure 27: 1460 keV peak counts by K content (% by mass)

Titanium content showed a linear relationship to thorium and uranium series activity. A plot of titanium content by mass against net peak counts for ^{212}Pb, ^{214}Pb, ^{214}Bi, and ^{228}Ac is shown in Figure 28. Groups of materials could be visually identified from this plot in terms of radioactivity in each region of interest and titanium content.
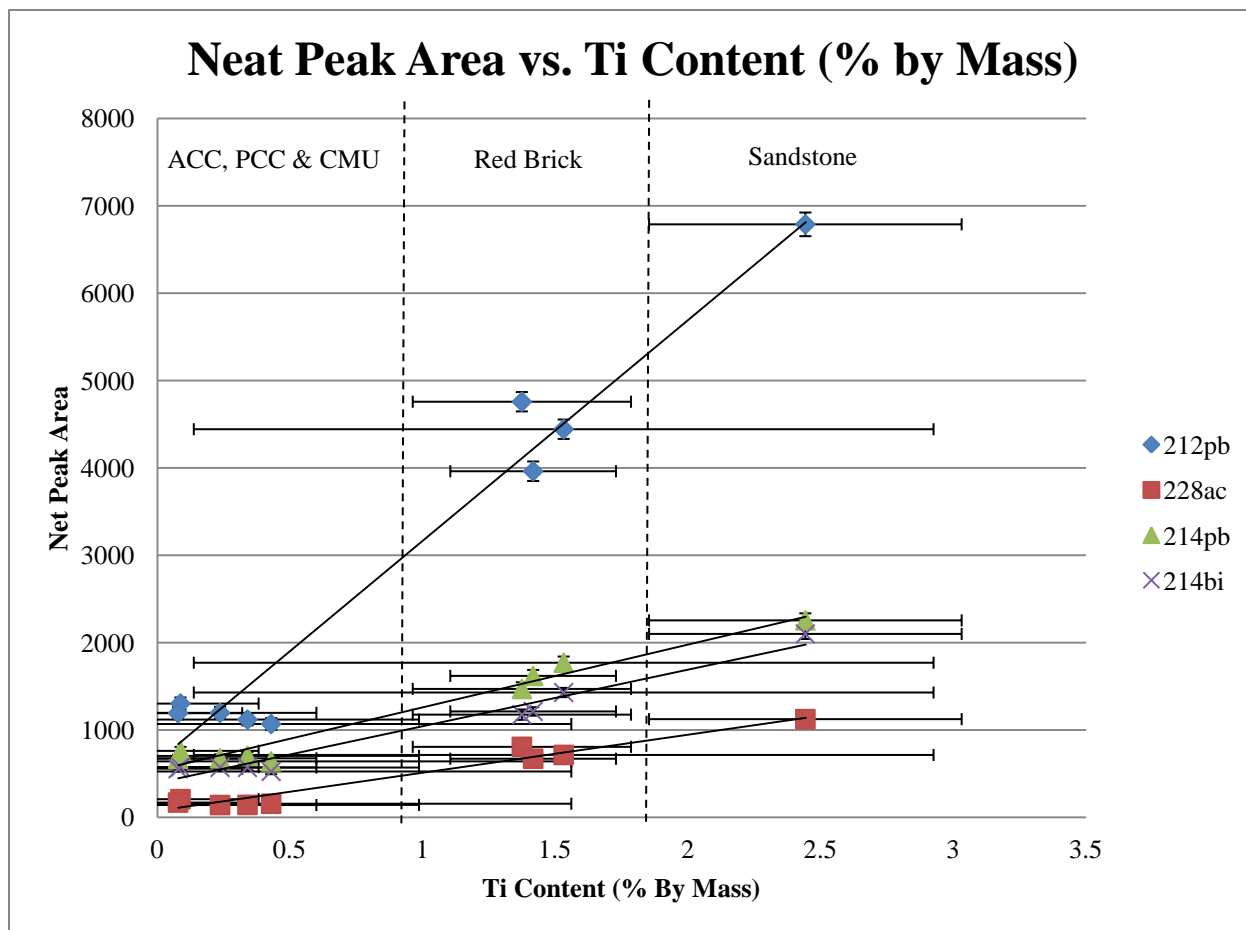
Figure 28: Thorium and uranium series peak counts by Ti content (% by mass)

Summary

An analysis was conducted on the data from each of the three sensors. Within each sensors data set, the various types of materials are distinguishable. Under gamma spectroscopy, the steel samples provided no background radiation. The concrete materials provided background radiation at low amounts for potassium, thorium, and uranium. The brick samples provided approximately twice the number of counts for uranium series as the concrete products. The difference in peak counts between concrete and brick was even greater for thorium and potassium. Sandstone provided the greatest

number of background counts in uranium and thorium series. In terms of counts originating from potassium, sandstone was similar to red brick.

The differences in peak areas at 1460 keV are explained by the difference in potassium content between the materials. The differences in thorium and uranium related counts are more complex. The radioactive progeny are not present in sufficient quantities to resolve under XRF analysis. In an unexpected result, each sample's titanium oxide count appears to be related linearly to thorium and uranium series counts.   Titanium oxide was more prevalent in samples with high amounts of silicates and lower in samples with largely composed of calcareous materials.

Hyper-spectral signatures within a group of materials, such as concrete, are very similar. Visual analyses of the absorption lines show that it is possible to distinguish brick from concrete and sandstone.

V. Conclusions and Recommendations

Chapter Overview

The purpose of this research was to analyze a selection of common construction materials in order to evaluate the potential value of hyper-spectral imagery as a tool for estimating background radiation in mobile nuclear detection applications in urban environments. This chapter provides the conclusion of this research effort. This conclusion includes the significance of the results described in Chapter IV for nuclear background modeling. Additionally, this chapter details areas for future research.

Conclusions of Research

As expected, the different types of construction materials were distinguishable by their hyper-spectral signatures. Distinguishing one material from another within a material type was more difficult through the qualitative analysis. Differences within material types may not be important to the larger problem of estimating background radiation. The gamma spectroscopy results showed that materials had similar radioactive properties within types. In terms of ^{212}Pb, ^{214}Pb, ^{214}Bi, ^{228}Ac, and ^{40}K, counts recorded from the Portland concrete were lower than counts recorded from brick and sandstone. Asphalt concrete had similar radioactive properties to Portland. The concretes are largely comprised of calcareous materials while the brick materials contain mostly silica sand. The relationship of titanium oxide to uranium and thorium series radioactivity in the samples could indicate that silica sand with titanium oxide in the local area contain uranium and thorium.

Significance of Research

This research forms a research baseline for methods to improve background correction in mobile detection application through the use of hyper-spectral imaging. This study identified relationships between construction material properties and background radiation which may warrant additional research.

Recommendations for Future Research

One of the primary limitations of this study is the small number sample materials. Future research should expand the number of samples within the material types and widen the variety of materials. This research is also regional. The materials are primarily from the Dayton Ohio local area. Future research should focus on materials from other regions. Chemical composition measurements could be improved by using pressed pill preparation techniques for the sample powders. Another limitation of this work is that it uses only point of contact instrumentation, which is not practical for mobile detection. In future work, measurements should be taken outdoors from a distance under a variety of lighting and weather conditions.

Appendix A

Materials

1. Steel
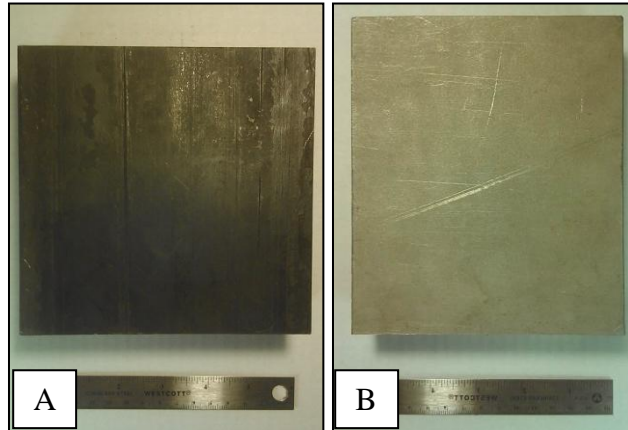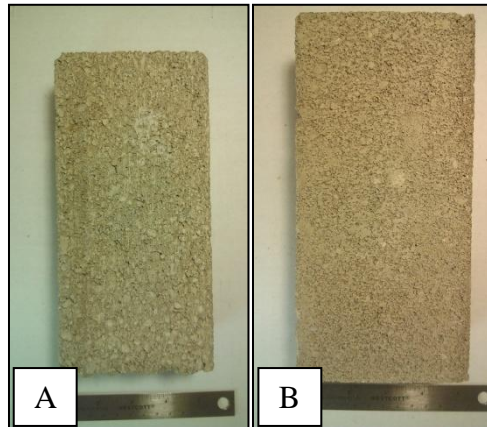

   a. A36: Alro Steel, Dayton Oh

   b. Stainless Steel: Alro Steel, Dayton Oh

2. ACC

   a. ACC #1: Wright-Patterson AFB, Oh

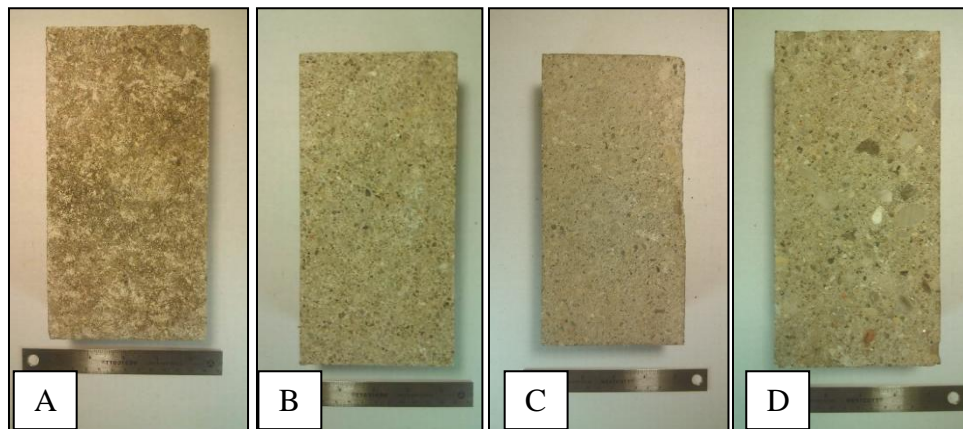3. CMU
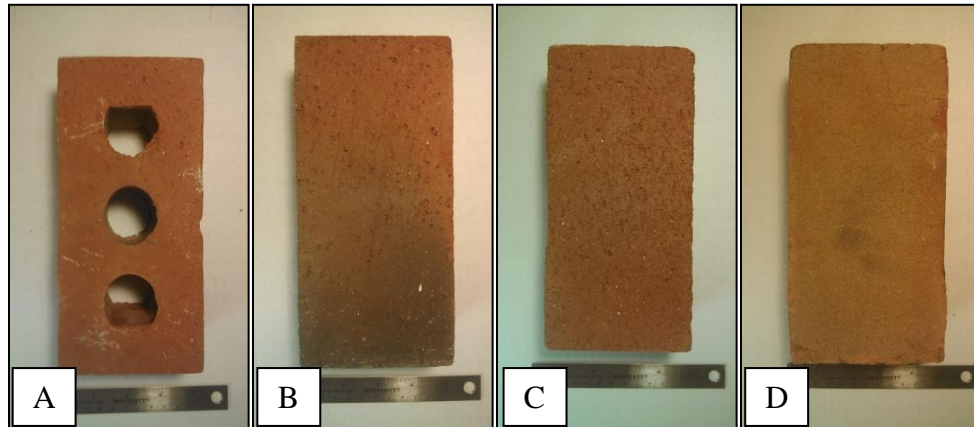

   a. CMU #1: Snyder Brick & Block, Dayton Oh

   b. CMU #2: Oberfields, Columbus Oh

4. Portland Concrete

   a. PCC #1: Wright-Patterson AFB, Oh

   b. PCC #2: Philips Sand & Gravel, Dayton Oh

   c. PCC #3: Philips Sand & Gravel, Dayton Oh

   d. PCC #4: Philips Sand & Gravel, Dayton Oh

5. Red Brick

   a. Red Brick #1: Discarded due to geometry, Wright-Patterson AFB, Oh

   b. Red Brick #2: Snyder Brick & Block, Dayton Oh

   c. Red Brick #3: Snyder Brick & Block, Dayton Oh

   d. Red Brick #4: Snyder Brick & Block, Dayton Oh

6. Sandstone
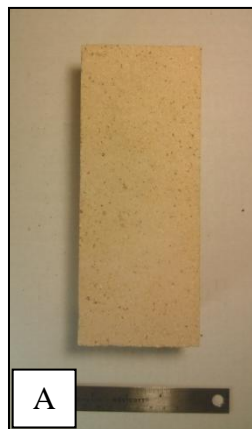
   a. Sandstone: Snyder Brick & Block, Dayton Oh

Appendix B

Horiba XGT-7000 Procedures

1. Check cryostat temperature.
   a. The detector must be cool to operate correctly.
   b. The temperature is indicated by the LN light on the front of the machine.
   c. Detector is cooled when LN light is GREEN.
   d. If the LN light is red, check the dewar liquid nitrogen level and fill as needed.
2. Open chamber and insert sample on test stand.
3. Activate vacuum system.
   a. Switch toggle on front of machine from Air to Vac.
4. Vacuum chamber.
   a. Press VAC C button on front of machine to start vacuum.
   b. Vacuum process is complete when VAC C light is GREEN.
5. Open XGT-7000 software.
   a. Create new project.
   b. Check that test stand is at lowest height.
   c. Conduct Origin Search.
   d. Photograph sample.
6. Focus Z-Axis.
   a. Start with height regulation camera view.
   b. Raise sample to height regulation line using control stick.
   c. Switch view to detail view.
   d. Observe sample through viewing window and carefully raise sample until the desired focus is achieved.
7. Set experiment parameters.
   a. Time: live time, 120s.
   b. Process time: larger process time provides improved resolution, 6.
   c. XGT: aperture size, 100 μm.
8. Start multi-point acquisition.
   a. Select grid.
   b. Set grid size: X = 3, Y=4.
   c. Select start.
9. Export data.
   a. Export spectra as EMSA.
   b. Export quantification results to EXCEL file.
10. Save project.
11. Remove sample.

a. Lower sample to lowest height.
b. In software, select Move to Exchange Position.
c. Press VAC C to release chamber vacuum.
d. Switch toggle from VAC to Air.
e. Open chamber door and remove sample.
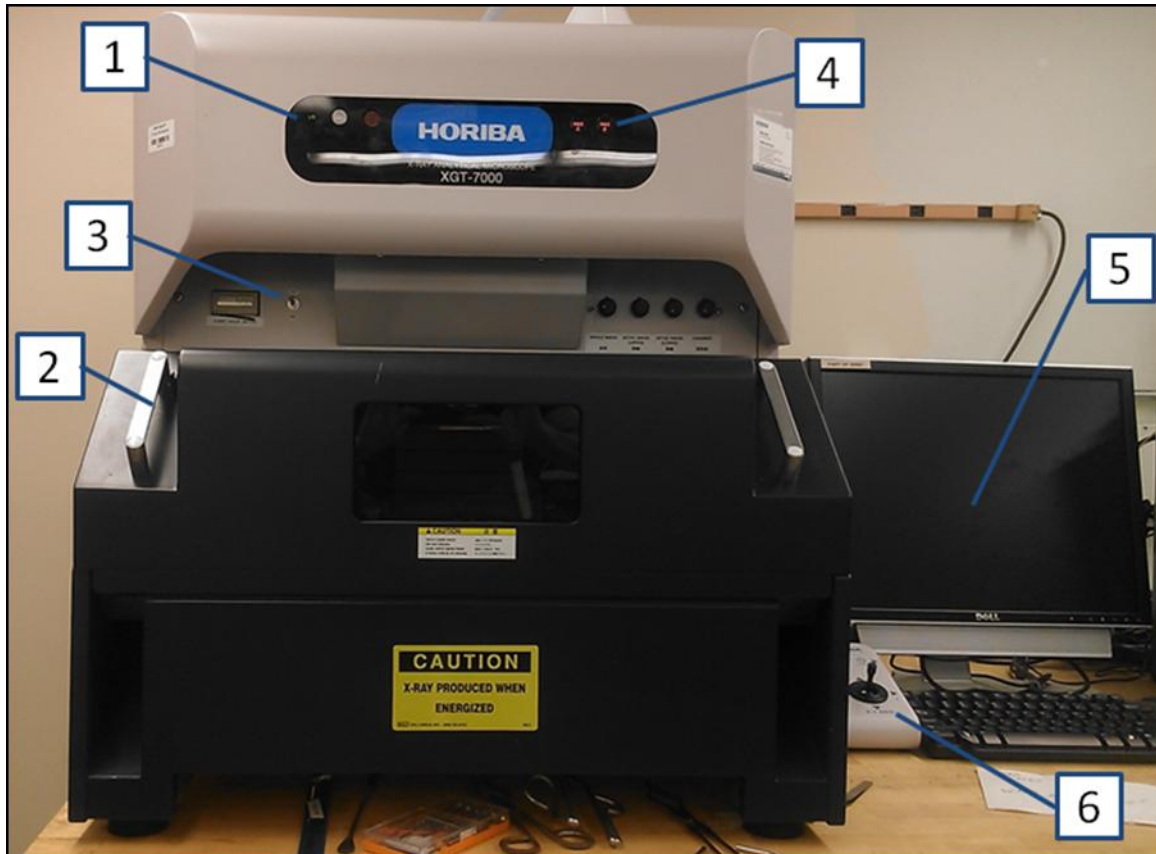
Bibliography

Asphalt Institute. (2003). *Principles of construction of hot-mix asphalt pavements* (No. 22, 2nd ed.), Lexington, Ky: Asphalt Institute.

ASTM. (1997). "Standard specification for carbon structural steel." *A36/ A36M-97a*, West Conshohocken, Pa.

ASTM. (2004). "Standard specification for tool steel high speed." *A600-92a*, West Conshohocken, Pa.

Aucott, T. J., Bandstra, M. S., Negut, V., Chivers, D. H., Cooper, R. J., & Vetter, K. (2013). Routine Surveys for Gamma-Ray Background Characterization. *Nuclear Science, IEEE Transactions on*, *60*(2), 1147-1150.

Chen, W. F., & Liew, J. R. (Eds.). (2003). *The civil engineering handbook* (2nd ed.). Boca Raton: CRC Press.

Cheng, J., Xie, M., Chen, R., & Roberts, F. S. (2011). *A latent model to detect multiple spatial clusters with application in a mobile sensor network for surveillance of nuclear materials*. Working paper, DIMACS Center, Rutgers University.

Clark, R. N. (1999), *Manual of Remote Sensing, Volume 3, Remote Sensing for the Earth Sciences*, (A.N. Rencz, ed.), New York, NY: John Wiley and Sons.

Dimitrov, N. B., Michalopoulos, D. P., Morton, D. P., Nehme, M. V., Pan, F., Popova, E., & Thoreson, G. G. (2009). Network deployment of radiation detectors with physics-based detection probability calculations. Annals of Operations Research, 187(1), 207-228.

Dzubay, T. G. (1977). X-ray fluorescence analysis of environmental samples. Ann Arbor Science Publishers.

Gredmaier, L., Banks, C. J., & Pearce, R. B. (2011). Calcium and sulphur distribution in fired clay brick in the presence of a black reduction core using micro X-ray fluorescence mapping. *Construction and Building Materials*, *25*(12), 4477-4486.

Huh, S., Maltz, J., Gunter, D., Mihailescu, L., & Vetter, K. (2012, October). Real-time radioactive source localization with a moving coded-aperture detector system at low count rates. In *Nuclear Science Symposium and Medical Imaging Conference (NSS/MIC), 2012 IEEE* (pp. 666-673). IEEE.

Jansson, P. A. (1984). *Deconvolution. with applications in spectroscopy*. New York, NY: Academic Press, 1984, edited by Jansson, Peter A.

Jones, D. R. (1993). *SHRP materials reference library: Asphalt cements: A concise data compilation* (Vol. 1). Washington, DC: Strategic Highway Research Program, National Research Council.

Knoll, G. F. (2010). *Radiation detection and measurement* (4th ed.). Hoboken, NJ: Wiley.

Kotright, J. B., & Thompson, A. C. (2009). X-ray Emission Energies. *X-ray Data Booklet*. Retrieved from http://xdb.lbl.gov/Section1/Sec_1-2.html

Liu, A. H., Bunn, J. J., & Chandy, K. M. (2011, April). Sensor networks for the detection and tracking of radiation and other threats in cities. In Information Processing in Sensor Networks (IPSN), 2011 10th International Conference on (pp. 1-12). IEEE.

Lo Presti, C. A., Weier, D. R., Kouzes, R. T., & Schweppe, J. E. (2006). Baseline suppression of vehicle portal monitor gamma count profiles: A characterization study. *Nuclear Instruments and Methods in Physics Research Section A: Accelerators, Spectrometers, Detectors and Associated Equipment*, *562*(1), 281-297.

Mitchell, L. J., Phlips, B. F., Johnson, W. N., Wulf, E. A., Roberts, R., Lister, C. J., & Guadagno, G. (2008, October). Mobile imaging and spectroscopic threat identification (MISTI). In *Nuclear Science Symposium Conference Record, 2008. NSS'08. IEEE* (pp. 642-647). IEEE.

Novikova, E. I., Phlips, B. F., & Wulf, E. A. (2007). A γ-ray background model for Monte Carlo simulations. *Nuclear Instruments and Methods in Physics Research Section A: Accelerators, Spectrometers, Detectors and Associated Equipment*, *579*(1), 279-283.

Philleo, R. E. (1989). Slag or other supplementary materials? Paper presented at the *Third International Conference on the Use of Fly Ash, Silica Fume, Slag and Natural Pozzolan in Concrete*, Trondheim, Norway.

Pfund, D. M., Runkle, R. C., Anderson, K. K., & Jarman, K. D. (2006, October). Examination of count-starved gamma spectra using the method of spectral comparison ratios. In *Nuclear Science Symposium Conference Record, 2006. IEEE* (Vol. 1, pp. 70-76). IEEE.

Rauckyte, T., Hargreaves, D. J., & Pawlak, Z. (2006). Determination of heavy metals and volatile aromatic compounds in used engine oils and sludges. *Fuel*, *85*(4), 481-485.

Tiwari, M. K., Singh, A. K., & Sawhney, K. J. S. (2001). Analysis of stainless steel samples by energy dispersive X-ray fluorescence (EDXRF) spectrometry. *Bulletin of Materials Science*, *24*(6), 633-638.

UNSCEAR, 1993. *United Nations Scientifc Committee on the Effects of Atomic Radiation, Exposure from Natural Sources of Radiation*. 1993 Report to the General Assembly.

Ekström, L.P., & Firestone, R.B. (2004, January). *WWW Table of Radioactive Isotopes*. Retreived from URL http://ie.lbl.gov/toi/index.htm.

Zaidi, J. H., Arif, M., Ahmad, S., Fatima, I., & Qureshi, I. H. (1999). Determination of natural radioactivity in building materials used in the Rawalpindi/Islamabad area by γ-ray spectrometry and instrumental neutron activation analysis. *Applied radiation and isotopes*, *51*(5), 559-564.

Zill, D. G., & Cullen, M. R. (1998). *Advanced engineering mathematics*. Sudbury, MA: Jones & Bartlett Publishers.

Ziock, K. P., Craig, W. W., Fabris, L., Lanza, R. C., Gallagher, S., Horn, B. K., & Madden, N. W. (2004). Large area imaging detector for long-range, passive detection of fissile material. *Nuclear Science, IEEE Transactions on*, 51(5), 2238-2244.

	Form Approved
REPORT DOCUMENTATION PAGE	OMB No. 074-0188

The public reporting burden for this collection of information is estimated to average 1 hour per response, including the time for reviewing instructions, searching existing data sources, gathering and maintaining the data needed, and completing and reviewing the collection of information. Send comments regarding this burden estimate or any other aspect of the collection of information, including suggestions for reducing this burden to Department of Defense, Washington Headquarters Services, Directorate for Information Operations and Reports (0704-0188), 1215 Jefferson Davis Highway, Suite 1204, Arlington, VA 22202-4302. Respondents should be aware that notwithstanding any other provision of law, no person shall be subject to any penalty for failing to comply with a collection of information if it does not display a currently valid OMB control number.
PLEASE DO NOT RETURN YOUR FORM TO THE ABOVE ADDRESS.

1. REPORT DATE *(DD-MM-YYYY)* 27 Mar 2014	2. REPORT TYPE Master's Thesis	3. DATES COVERED *(From – To)* Oct 2012 – Mar 2014

4. TITLE AND SUBTITLE Characterization of Construction Material Properties through Gamma Spectroscopy, X-ray Fluorescence, and Hyper-spectral Imagery for Background Correction Applications in Nuclear Detection	5a. CONTRACT NUMBER
	5b. GRANT NUMBER
	5c. PROGRAM ELEMENT NUMBER

6. AUTHOR(S) Casebolt, Jared D., Captain, USAF	5d. PROJECT NUMBER JON13P166
	5e. TASK NUMBER
	5f. WORK UNIT NUMBER

7. PERFORMING ORGANIZATION NAMES(S) AND ADDRESS(S) Air Force Institute of Technology Graduate School of Engineering and Management (AFIT/ENV) 2950 Hobson Way, Building 640 WPAFB OH 45433-8865	8. PERFORMING ORGANIZATION REPORT NUMBER AFIT-ENP-14-M-45

9. SPONSORING/MONITORING AGENCY NAME(S) AND ADDRESS(ES) Defense Threat Reduction Agency Dr. David Peterson 8725 John Kingman Rd Ft. Belvoir, VA 22060 (7030 767-3164 david.peterson@dtra.mil	10. SPONSOR/MONITOR'S ACRONYM(S) DTRA
	11. SPONSOR/MONITOR'S REPORT NUMBER(S)

12. DISTRIBUTION/AVAILABILITY STATEMENT
DISTRIBUTION STATEMENT A: APPROVED FOR PUBLIC RELEASE; DISTRIBUTION UNLIMITED

13. SUPPLEMENTARY NOTES
This material is declared a work of the U.S. Government and is not subject to copyright protection in the United States.

14. ABSTRACT
Material identification through hyper-spectral imagery provides a potentially useful data input for background radiation prediction models for gamma spectrum correction in mobile nuclear detection applications. Traditional background correction methods which rely on prior information are often impractical in mobile detection. Prediction models could combine material information with spatial data to develop a suitable substitute to actual background radiation measurements. This research investigates the relationship hyper-spectral properties and natural radioactivity of construction materials. A selection of construction materials are analyzed using three instrumentation methods: 1) gamma-spectroscopy, 2) X-ray fluorescence (XRF), and 3) hyper-spectral imagery. Gamma-spectroscopy focuses on the presence of potassium as well as uranium and thorium series progeny through analysis of 212Pb, 214Pb, 214Bi, and 228Ac signature peaks. XRF analysis provides the chemical composition of each material. Each materials hyper-spectral characteristics are compared to chemical composition and radioactive properties to determine if any identifying features relate to natural radioactivity.

15. SUBJECT TERMS
Nuclear detection, X-ray fluorescence, Gamma-spectroscopy, Hyper-spectral imaging

16. SECURITY CLASSIFICATION OF:			17. LIMITATION OF ABSTRACT	18. NUMBER OF PAGES	19a. NAME OF RESPONSIBLE PERSON David J. Bunker, PhD, USAF
a. REPORT	b. ABSTRACT	c. THIS PAGE	UU or SAR	88	19b. TELEPHONE NUMBER *(Include area code)* (937) 255-6565, x 4547 (david.bunker@afit.edu)
U	U	U			

Standard Form 298 (Rev. 8-98)
Prescribed by ANSI Std. Z39-18